

Supporting Information

Unveiling the Reaction Mechanism of Capacity Reactivation in Silver Vanadate Cathode for Aqueous Zinc-Ion Batteries

Ziqing Wang,^a Jiefeng Diao,^{ab} Kenta Kawashima,^a Jason A. Weeks,^a Rinish Reddy Vaidyula,^a Raul A. Marquez,^a Nathaniel Miller,^c Graeme Henkelman,^{ab} and C. Buddie Mullins^{*ade}

^a Department of Chemistry, The University of Texas at Austin, Austin, Texas 78712, United States

^b Oden Institute for Computational Engineering and Sciences, The University of Texas at Austin, Austin, Texas 78712, United States

^c Department of Geosciences, The University of Texas at Austin, Austin, Texas 78712, United States

^d Texas Materials Institute, The University of Texas at Austin, Austin, Texas 78712, United States

^e McKetta Department of Chemical Engineering, The University of Texas at Austin, Austin, Texas 78712, United States

* Corresponding author: mullins@che.utexas.edu

Experiments:

Material Synthesis

Synthesis of $\text{Ag}_{0.33}\text{V}_2\text{O}_5$: $\text{Ag}_{0.33}\text{V}_2\text{O}_5$ (AgVO) was synthesized by a one-step hydrothermal method. First, 0.3 g V_2O_5 was dissolved in 30 mL deionized water, and then the mixture was heated to 50 °C. Subsequently, 4 mL H_2O_2 (30%) was added dropwise into the above solution. After stirring for 20 min at 50 °C, 28.0 mg AgNO_3 was added into the above solution for a further 20 min stirring. Afterward, the mixed solution was transferred into a 50 mL Teflon-lined autoclave and heated at 225 °C for 48 h. After cooling down to room temperature, the products were collected and washed with ethanol and deionized water 3 times and then dried in the vacuum oven at 60 °C for 12 h.

Synthesis of $\text{Na}_{0.33}\text{V}_2\text{O}_5$: NaVO cathode material was synthesized via a hydrothermal method based on the previous literature.¹ Briefly, 0.1818 g V_2O_5 was dissolved in the solution of 30 mL deionized (DI) water with the addition of 0.014 g NaOH in a beaker. After 5 min stirring, 0.1 g PEG-4000 was added into the above solution with continuous stirring at room temperature for 15 min. After that, the mixture was transferred to a 50 mL Teflon-lined autoclave and heated at 180 °C for 48 h. Afterward, the system was cooled down to room temperature naturally and the samples were washed with deionized water and ethanol three times each. The final product was dried at 60 °C for 8 h under vacuum, and the green-yellow powder was obtained.

Synthesis of $\text{Zn}_3(\text{OH})_2\text{V}_2\text{O}_7 \cdot 2\text{H}_2\text{O}$: ZnVO cathode material was synthesized based on a hydrothermal method based on the previous report.² Briefly, 7.5 mmol NH_4VO_3 powder was dissolved in 20 mL DI water at 80 °C (solution A). After 20 minutes, 5 mmol glycine was added to the solution. At the same time, another 5 mmol $\text{Zn}(\text{NO}_3)_2 \cdot 6\text{H}_2\text{O}$ was added into 10 mL DI water (solution B). Afterward, solution A was added to solution B drop by drop and the mixture was stirred for 10 minutes. Finally, the mixture was transferred into a 50 mL Teflon-lined autoclave and heated at 180 °C for 8 h. The final product was washed with DI water three times and dried under vacuum overnight.

Synthesis of V_2O_5 : V_2O_5 was synthesized by the same hydrothermal method as AgVO without the addition of AgNO_3 . First, 0.3 g V_2O_5 was dissolved in 30 mL deionized water and then the mixture was heated to 50 °C. Subsequently, 4 mL H_2O_2 (30%) was added dropwise into the above solution, and the mixture was stirred for 20 min at 50 °C. Afterward, the mixed solution was

transferred into a 50 mL Teflon-lined autoclave and heated at 225 °C for 48 h. After cooling down to room temperature, the products were collected and washed by ethanol and deionized water for 3 times each and then dried in the vacuum oven at 60 °C for 12 h.

Material Characterization

Before checking the crystalline structure of AgVO, it is necessary to ground the orange product into small powder. Powder X-ray diffraction (PXRD) was applied to evaluate the crystallinity of AgVO by Rigaku MiniFlex 600 (Cu K α radiation, $\lambda = 1.5418 \text{ \AA}$) with the scan rate of 2° min $^{-1}$. All the electrodes were also characterized by Rigaku MiniFlex 600. Transmission electron microscopy (TEM) and high-resolution transmission electron microscopy (HRTEM) were conducted by a JEOL NEOARM instrument to reveal the nanostructural phase transition. The morphological information of AgVO and cathodes was obtained *via* scanning electron microscopy (SEM) by FEI Quanta 650 and Hitachi S-5500 SEM/STEM. X-ray photoelectron spectroscopy (XPS) analysis was carried on by a Kratos Axis Ultra X-ray photoelectron spectrometer. The contact angle was measured by a FTA200 contact angle goniometer. Electrolyte composition was tested by solution-mode ICP-MS applying an Agilent 7500ce with a collision reaction cell (He and H₂ modes).

Electrochemical Measurement

The cathodes were prepared by mixing AgVO active material, super P, and polyvinylidene fluoride (PVDF) with a mass ratio of 7:2:1. The powder mixture was grounded for 20 min until uniform. The proper amount of N-methyl-2-pyrrolidone (NMP) was dropped into the mixture for continuous 20 min grounding until the black slurry became even enough. The slurry was coated on the 500-mesh stainless-steel wire mesh with average active material mass loading of 1 mg cm $^{-2}$ with the following overnight drying at 70 °C under vacuum. The coin cells were assembled in 2032 coin cell cases at ambient atmosphere using the as-prepared AgVO electrode as a cathode, glass fiber as a separator, 0.1 mm thick Zn metal as an anode, and 3 M Zn(ClO₄)₂ and 3 M ZnSO₄ as electrolyte. Cycling performance at different current densities was performed *via* a multichannel battery test system (Neware BTS4000-5V10mA) at 0.4-1.4 V. Cyclic voltammetry (CV) tests and

electrochemical impedance spectrometry (EIS) were performed on a CHI 608D electrochemical workstation.

DFT Calculations

Density functional theory (DFT) calculations were performed using the generalized gradient approximation (GGA), Perdew-Burke-Ernzerhof (PBE) functional, and projected augmented plane-wave method implemented in the Vienna ab initio simulation package (VASP). In our DFT calculations, the plane wave basis set cutoff of the wavefunctions were set at 400 eV, and the zero damping DFT-D3 method was used to describe weak intermolecular (dispersion) interactions. All energy data collected were after a full relaxation of the systems until the forces on each atom were less than 0.01 eV/Å. Structure models were all drawn with VESTA. The partial density of states (PDOS) of $\text{Zn}_3(\text{OH})_2\text{V}_2\text{O}_7 \cdot 2\text{H}_2\text{O}$ was obtained from a calculation with a primitive cell containing 3 Zn, 11 O, 2 V, and 6 H atoms. Transition states of interest were found using the CI-NEB method.

Capacitance contribution calculations:

The CV curves at 0.2-1.0 mV s⁻¹ were tested to calculate the capacitance contribution. Two redox peaks can be found in the CV curves. The relationship between peak currents (*i*) and scan rates (*v*) is shown as below:³

$$i = av^b$$

The equation can be changed into:

$$\log(i) = b\log(v) + \log(a)$$

where *b* represents the slope of the log(*i*)-log(*v*) curve. The capacitive contribution can be calculated by the equation:

$$i = k_1v + k_2v^{1/2}$$

The above equation can be transformed into:

$$i/v^{1/2} = k_1v^{1/2} + k_2$$

in which *i*, k_1v , and $k_2v^{1/2}$ represent current, the contribution of capacitance, and the contribution of ionic diffusion, respectively.

Electrochemically active surface areas (ECSAs) calculations:

The electrochemically active surface areas (ECSAs) were estimated from the electrochemical double layer capacitance (C_{dl}). Double layer capacitance measurement was carried out by a three-electrode system in 1 M KOH solution. AgVO cathodes before and after 50 cycles, a graphite rod, and a Hg/HgO electrode in 1 M KOH were utilized as working, counter, and reference electrode, respectively.

CV in a non-faradaic potential range of 0.05-0.10 V_{Hg/HgO} was carried out at eight different scan rates (10, 25, 50, 100, 150, 200, 250, and 500 mV s⁻¹) to calculate the C_{dl} of AgVO cathodes before and after reactivation from the scan rate dependence of double layer charging [$\Delta i/2 = (i_a - i_c)/2$].

The tested geometric surface area (S_t) of the cathode is 0.196 cm², and the real geometric surface area (S_r) of the cathode is 1.327 cm², the relationship between C_{dl} and the ECSA can be calculated by the following equation:

$$ECSA = \frac{C_{dl}}{S_t \times C_s} \times S_r$$

In which the C_{dl} is the slope of the fitting curve in Fig. S33c and d, and the C_s is the general specific capacitance ($C_s = 0.040$ mF cm⁻²) in 1 M KOH.^{4,5}

GITT calculations:

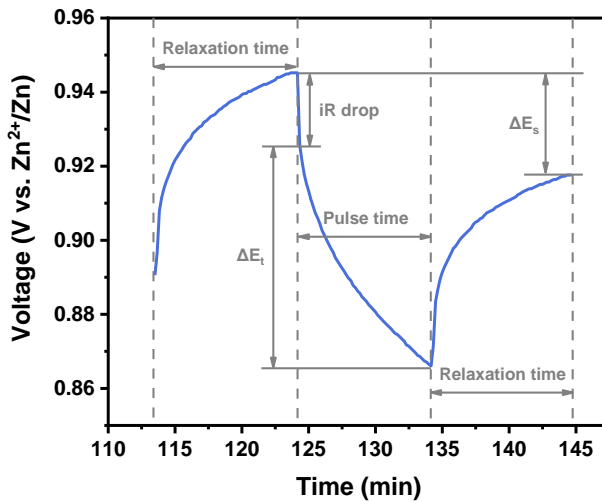


Fig. 1. Voltage vs. time curve of AgVO cathode for a single GITT during the discharge process.

The diffusion coefficient was measured by Galvanostatic Intermittent Titration Technique (GITT) and calculated by the equations shown as below:^{6,7}

$$D = \frac{4L^2}{\pi\tau} \left(\frac{\Delta E_s}{\Delta E_t} \right)^2$$

Where t is the duration of the current pulse (s), τ is the relaxation time (s), ΔE_s is the steady-state potential change (V), and ΔE_t is the potential change (V) during the constant current pulse after eliminating the iR drop, L is the diffusion length of Zn²⁺, which equals to the thickness of the cathode material on the current collector.

Activation energy calculation:

Nyquist plots of AgVO cathodes in 3 M Zn(ClO₄)₂ and 3 M ZnSO₄ were carried out under different temperatures (i.e., 5, 10, 20, and 30 °C). The interface resistances (R_{ct}) were obtained by electrochemical impedance spectroscopy (EIS) fitting.

From the Arrhenius equation:

$$k = A e^{-\frac{E_a}{RT}}$$

in which k is the rate constant of the reaction, A is the Arrhenius constant, E_a is the activation energy of the reaction, R is the gas constant; T is the thermodynamic temperature (K).

The Arrhenius equation can be turned into:

$$\ln k = -\frac{E_a}{RT} + \ln A$$

in which the rate constant k is $1/R_{ct}$, by linear fitting $\ln 1/R_{ct}$ and $1/T$, the activation energy of each reaction can be obtained.⁸

Supplementary figures:

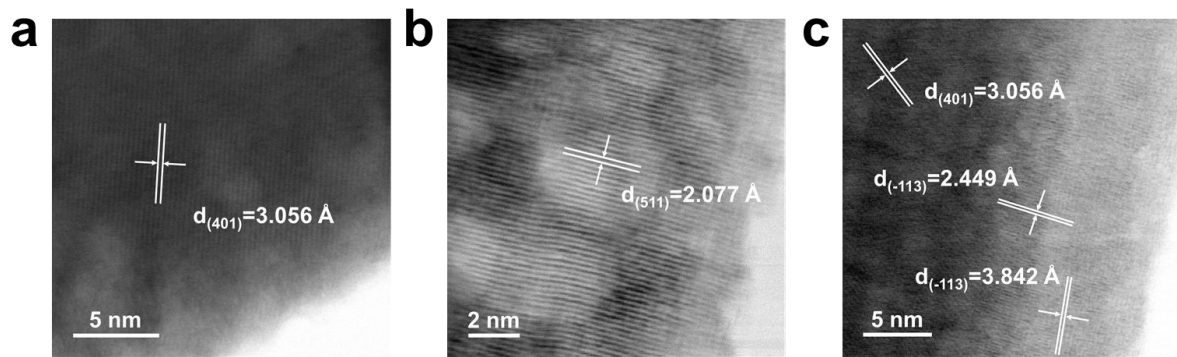


Fig. S1. HRTEM images of AgVO powder.

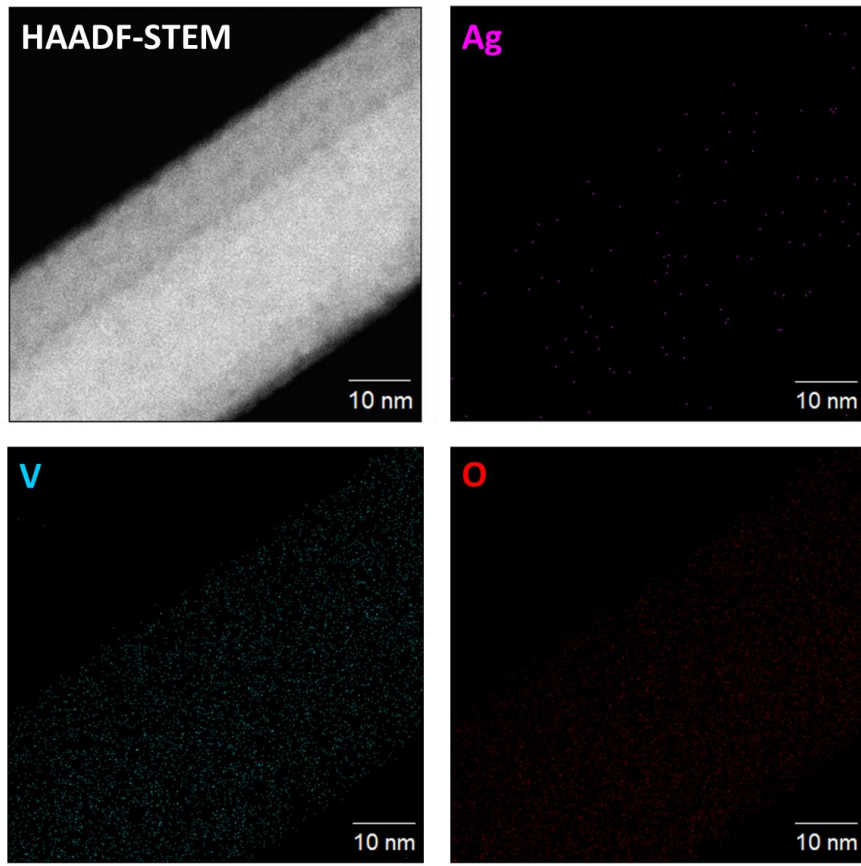


Fig. S2. HAADF-STEM element mapping images of AgVO nanobelt.

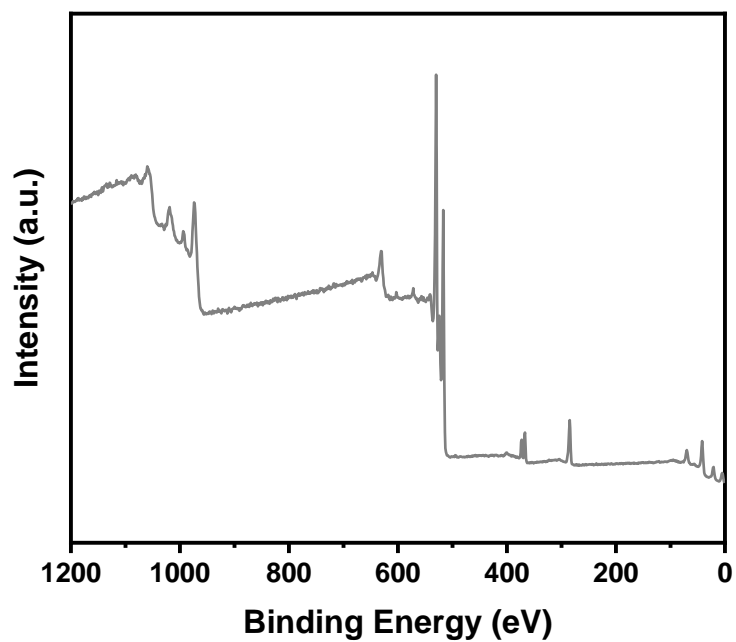


Fig. S3. XPS survey spectrum of the AgVO material.

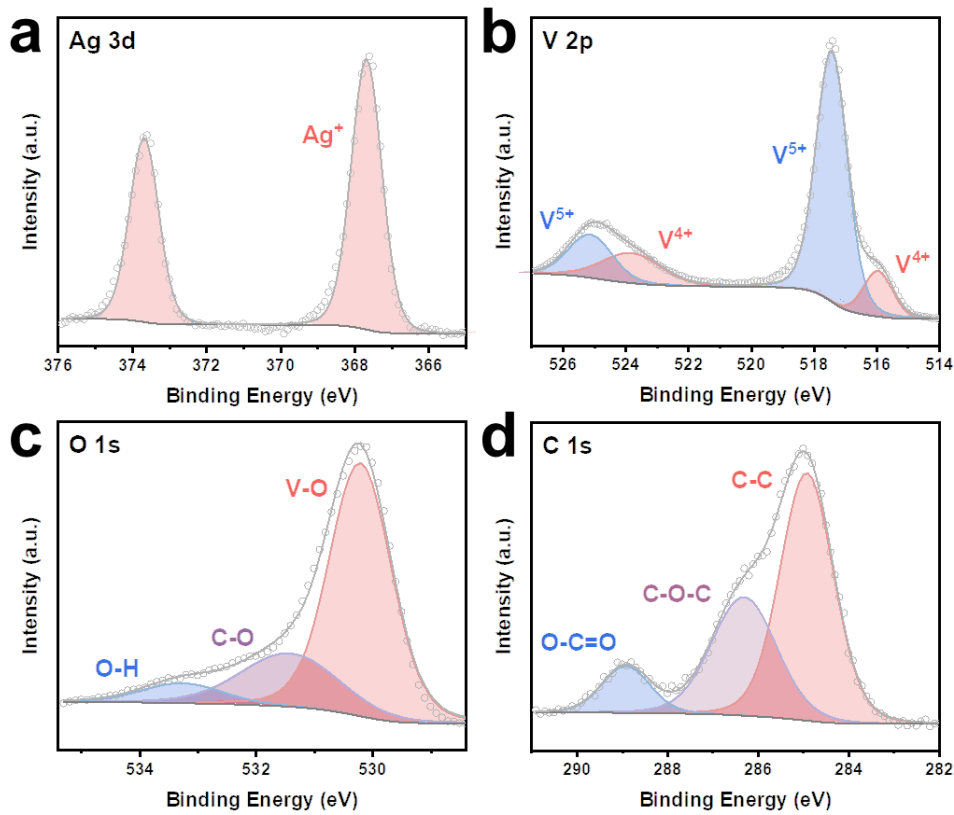


Fig. S4. XPS spectra of (a) Ag 3d, (b) V 2p, (c) O 1s, and (d) C 1s of AgVO powder.

In Fig. S4c and S4d, the C–C, C–O, and C=O components are from the adventitious carbon contamination during materials synthesis.⁹ The carbonates in the atmosphere adsorbed on the materials' surface, which causes the detection of C signal in the XPS spectra. In addition, the C–C component in Fig. S4d at 284.8 eV was used as a reference peak to calibrate the whole spectra.

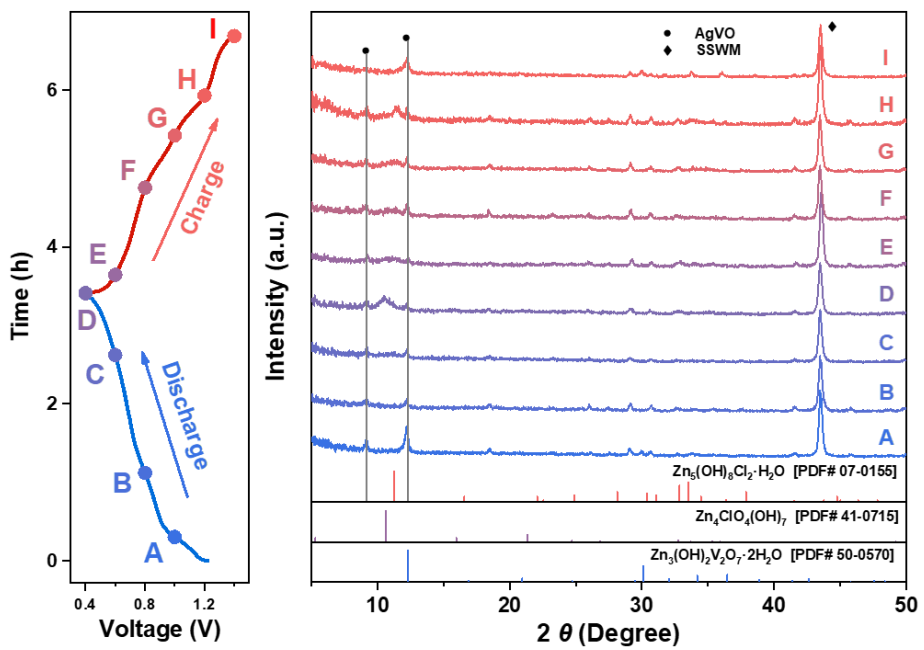


Fig. S5. *Ex situ* XRD patterns of AgVO/Zn batteries using 3 M $Zn(ClO_4)_2$ at the first cycle.

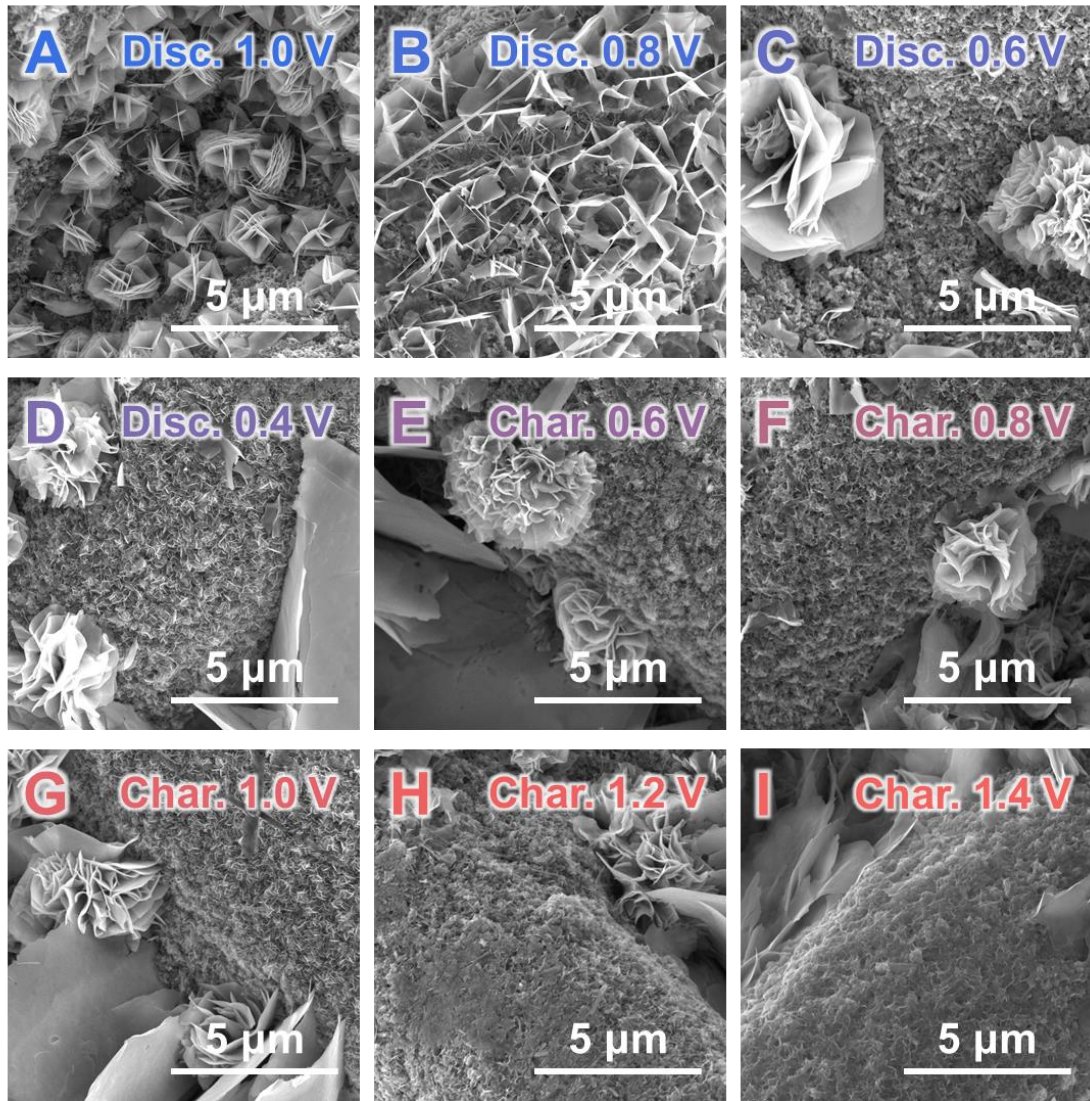


Fig. S6. SEM images at different discharge/charge states corresponding to the *ex situ* XRD patterns.

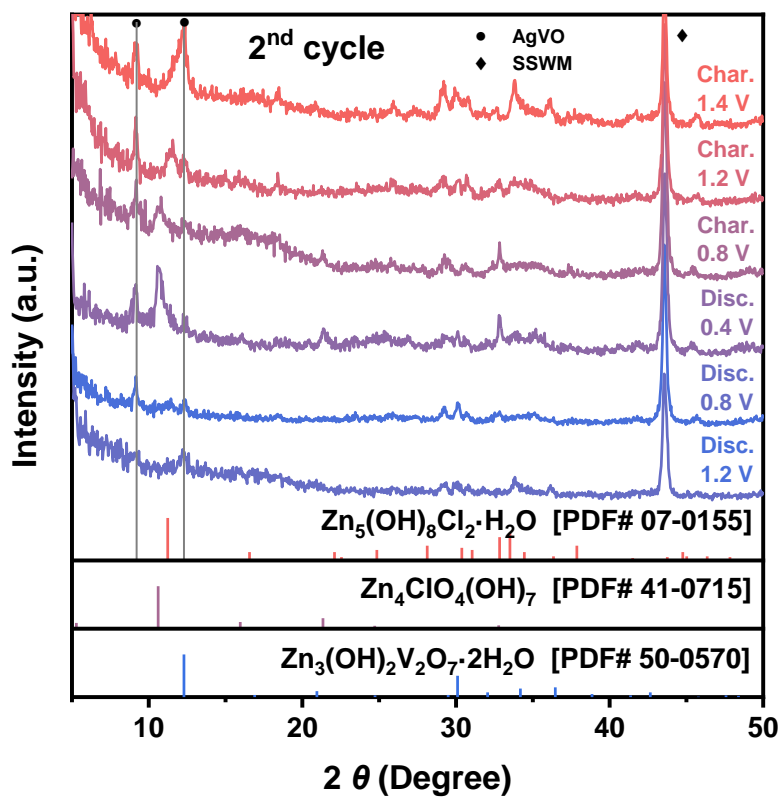


Fig. S7. *Ex situ* XRD patterns of AgVO/Zn batteries using 3 M $\text{Zn}(\text{ClO}_4)_2$ at the second cycle.

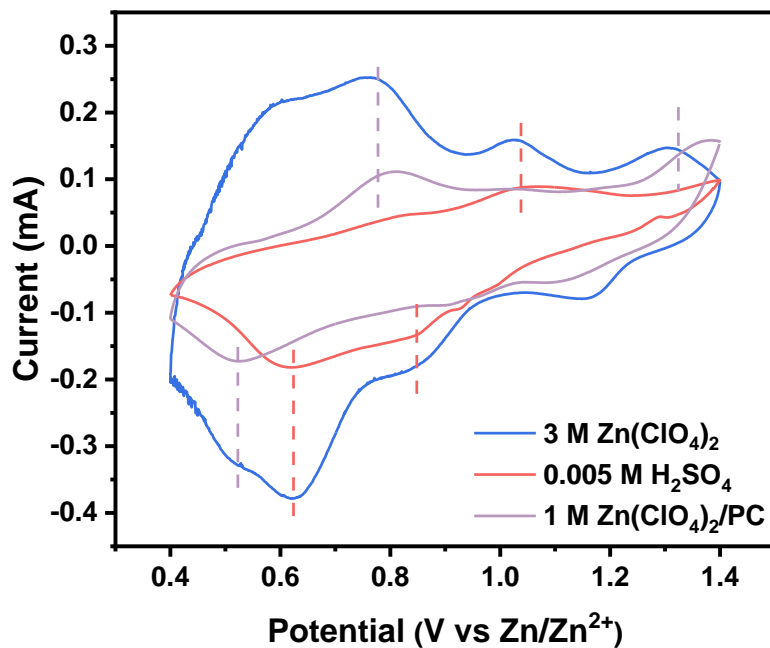


Fig. S8. CV curves of AgVO/Zn batteries using different electrolytes.

In order to reveal the insertion of Zn^{2+} and H^+ , the cyclic voltammetry (CV) plots of AgVO/Zn batteries using 3 M $\text{Zn}(\text{ClO}_4)_2$, 1 M $\text{Zn}(\text{ClO}_4)_2$ in propylene carbonate (PC), and 0.005 M H_2SO_4 electrolytes are compared and analyzed (Fig. S8). In the CV curve of the battery using the 0.005 M H_2SO_4 electrolyte, the peaks located at 0.85 V and 0.62 V during the cathodic sweep, which can be ascribed to the H^+ insertion, cannot be found in the non-aqueous electrolyte (1 M $\text{Zn}(\text{ClO}_4)_2/\text{PC}$). On the contrary, the peak at 0.51 V in the cathodic sweep in the non-aqueous battery belongs to the insertion of Zn^{2+} . The above results show a similar trend that has been reported in the previous literature suggesting that the major intercalated cations gradually change from H^+ to Zn^{2+} during discharge.^{10,11} During an anodic sweep, the peaks at 0.8 V and 1.3 V in the non-aqueous battery represent the extraction of Zn^{2+} , while the peak at 1.0 V corresponds to the deintercalation of H^+ .

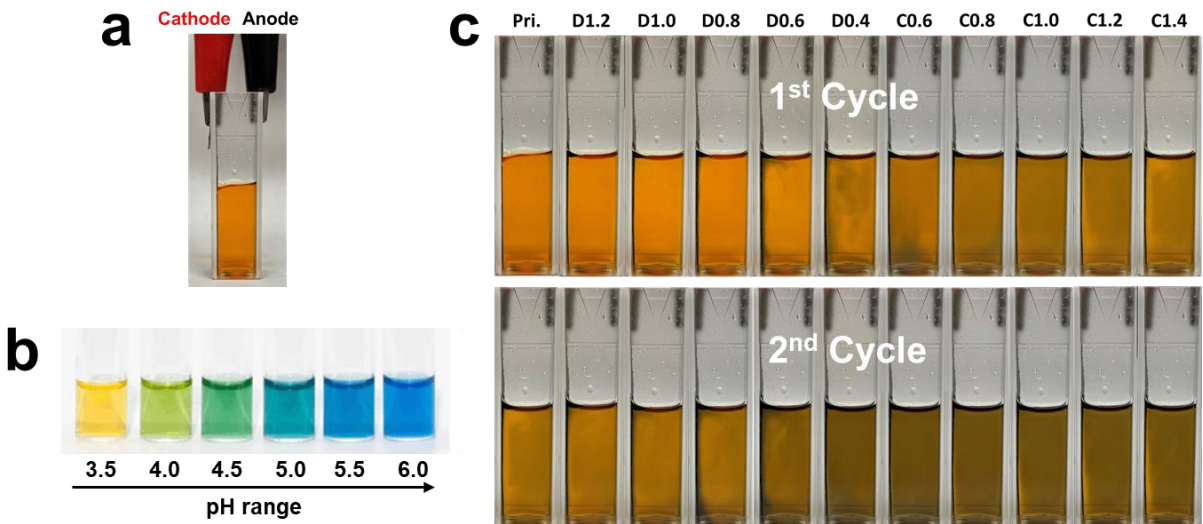


Fig. S9. (a) Schematic of the cuvette pH test cell. (b) pH color chart of bromocresol green at different pH. (c) *Ex situ* pH color change of AgVO/Zn battery using 3 M $\text{Zn}(\text{ClO}_4)_2$ electrolyte in the first 2 cycles.

The resulting pH change from the insertion and extraction of H^+ was investigated by cycling a AgVO/Zn cell in a cuvette with indicator bromocresol green present (Fig. S9a and b). The *in situ* pH change was monitored through the colorimetric indication at various voltages (Fig. S9c). The 3 M $\text{Zn}(\text{ClO}_4)_2$ electrolyte, which has a pH of 2.85, near the cathode surface turns to dark green upon discharge to 0.8 V and changes back to orange upon charge to 0.8V, representing a reversible pH increase and decrease, respectively, which corresponds to the insertion/extraction of proton in the cathode. Because of the insertion of H^+ in the cathode, the remaining water decomposition product OH^- participated in the formation of $\text{Zn}_5(\text{OH})_8\text{Cl}_2 \cdot \text{H}_2\text{O}$ and $\text{Zn}_4\text{ClO}_4(\text{OH})_7$.

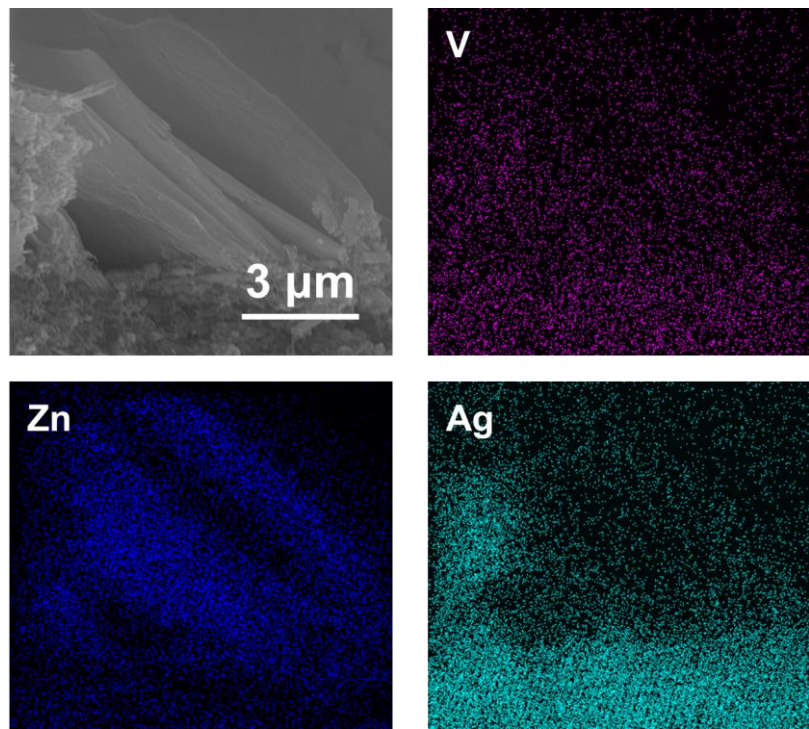


Fig. S10. SEM image and corresponding EDX elemental mapping images of V, Zn, and Ag of the cathode cycled for 10 cycles at 0.1 A g^{-1} .

The SEM image shows the coverage of nanosheets on the cathode surface. The corresponding EDX results displayed an even distribution of V signal in the mapping, indicating that both the original cathode and newly formed nanosheets contain V. However, the Zn signal can only be observed in the surface nanosheets and the Ag signal only emerged in the substrate cathode material, which means the substrate is original AgVO, and the nanosheets on the surface are ZnVO.

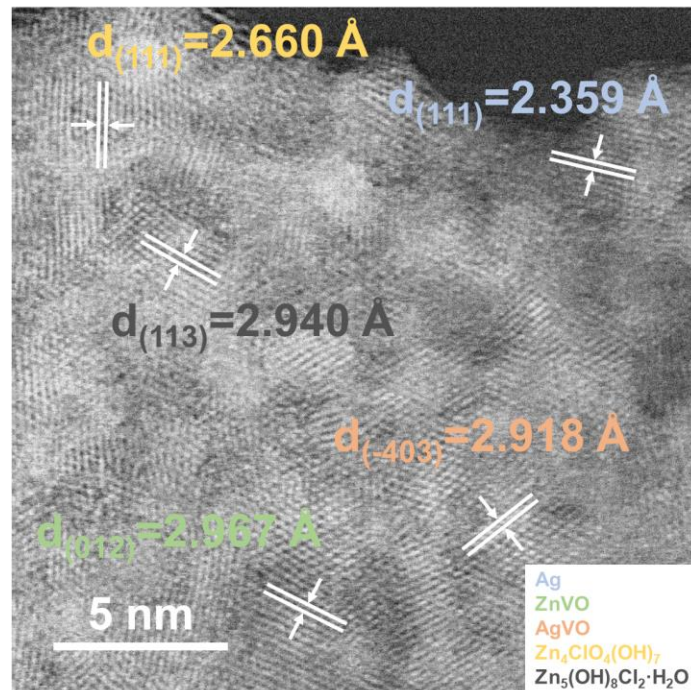


Fig. S11. HRTEM image of the cathode after fully charged in the first cycle.

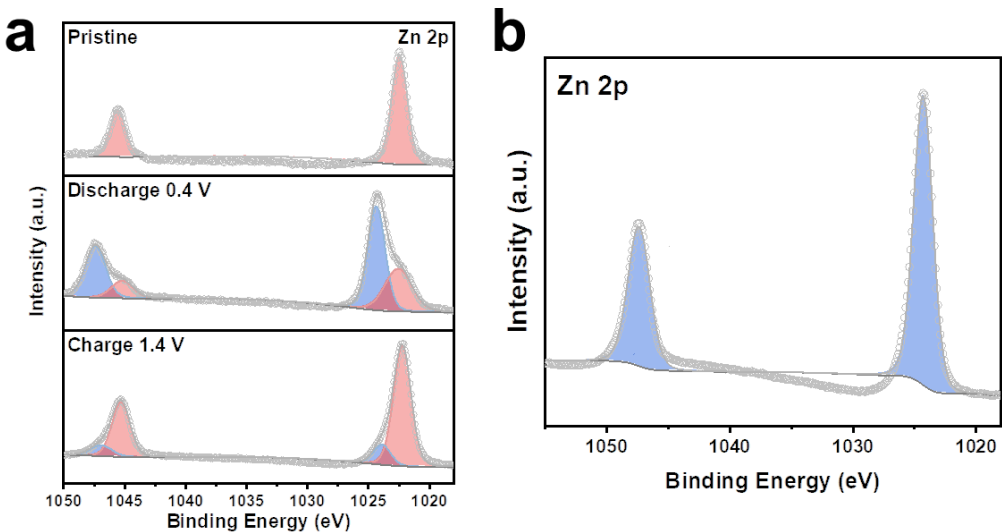


Fig. S12. (a) XPS spectra of Zn 2p of the hydrothermal-synthesized ZnVO cathodes in the first cycle. (b) XPS spectra of Zn 2p of $\text{Zn}(\text{OH})_2$.

Fig. S12a shows the XPS result of the hydrothermal-synthesized ZnVO after the 1st discharging and charging. The peaks at 1022.4 and 1045.2 eV can be ascribed to the pristine ZnVO. After discharging to 0.4 V, the peaks at 1024.4 and 1047.5 eV assigned to the Zn^{2+} inserted into the ZnVO were observed. Moreover, as shown in Fig. S12b, the Zn 2p XPS result of $\text{Zn}(\text{OH})_2$ indicates the peaks at 1024 and 1047 eV can also be ascribed to zinc hydroxide byproducts.

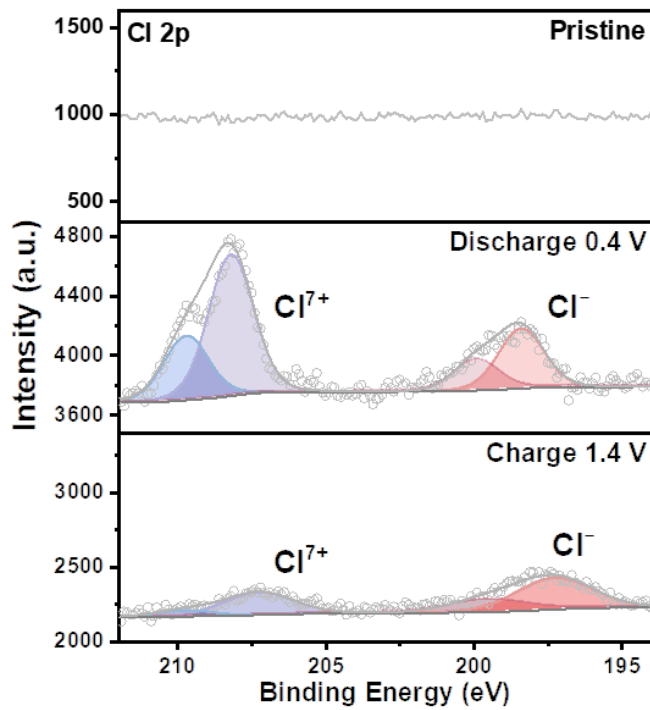


Fig. S13. XPS spectra of Cl 2p of the AgVO cathodes in the first cycle.

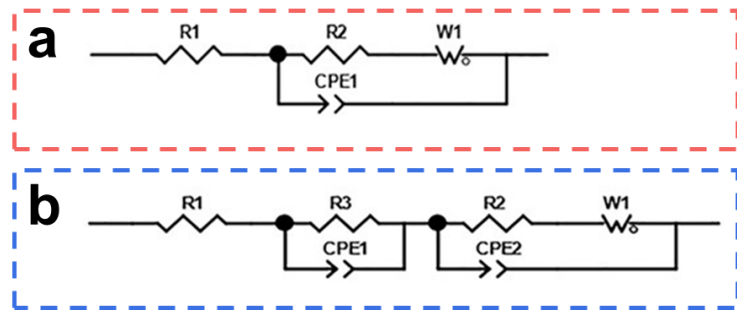


Fig. S14. Equivalent circuits to the Nyquist plots of (a) 3 M ZnSO₄ and (b) 3 M Zn(ClO₄)₂.

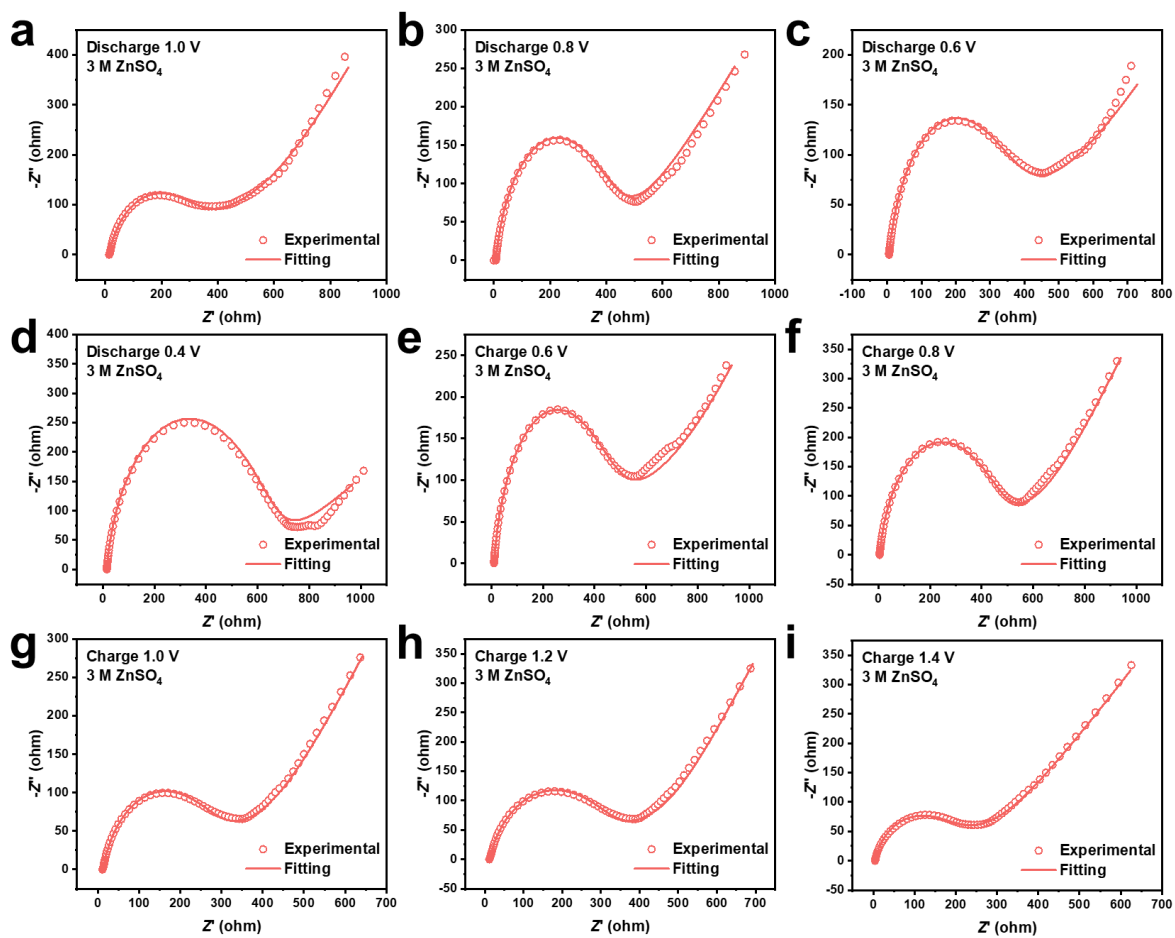


Fig. S15. Nyquist plots and fitting curves of the batteries in 3 M ZnSO_4 at different discharge/charge states.

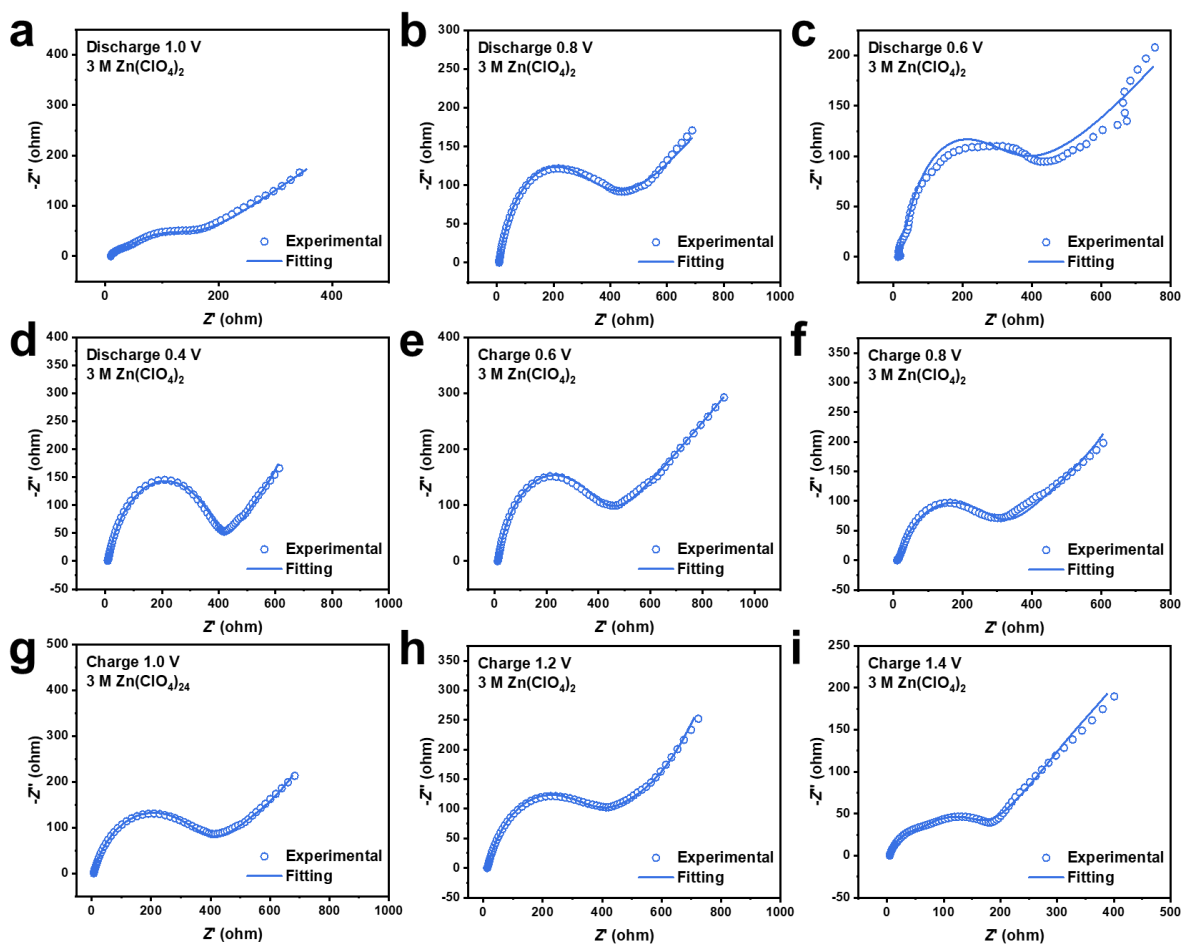


Fig. S16. Nyquist plots and fitting curves of the batteries in 3 M $\text{Zn}(\text{ClO}_4)_2$ at different discharge/charge states.

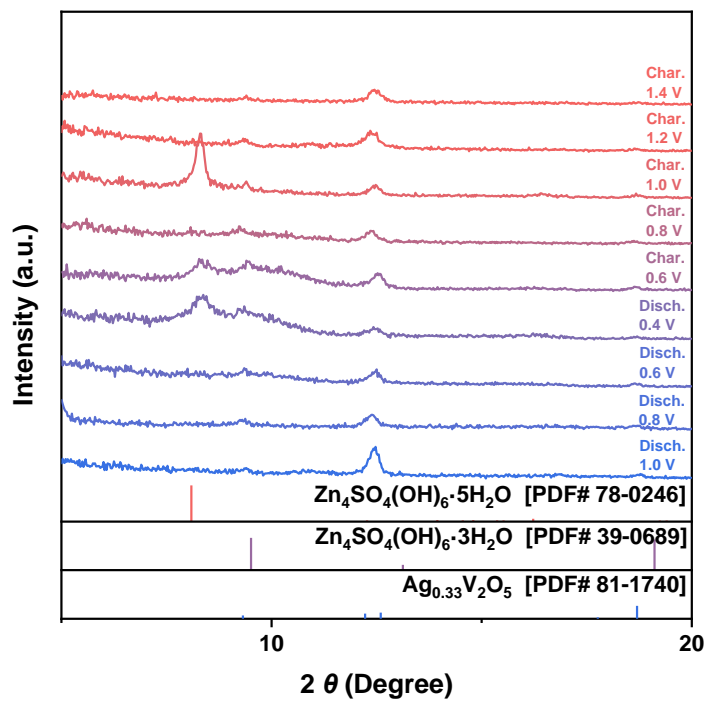


Fig. S17. *Ex situ* XRD patterns of the AgVO cathodes during the first cycle in 3 M ZnSO₄ electrolyte at 0.1 A g⁻¹.

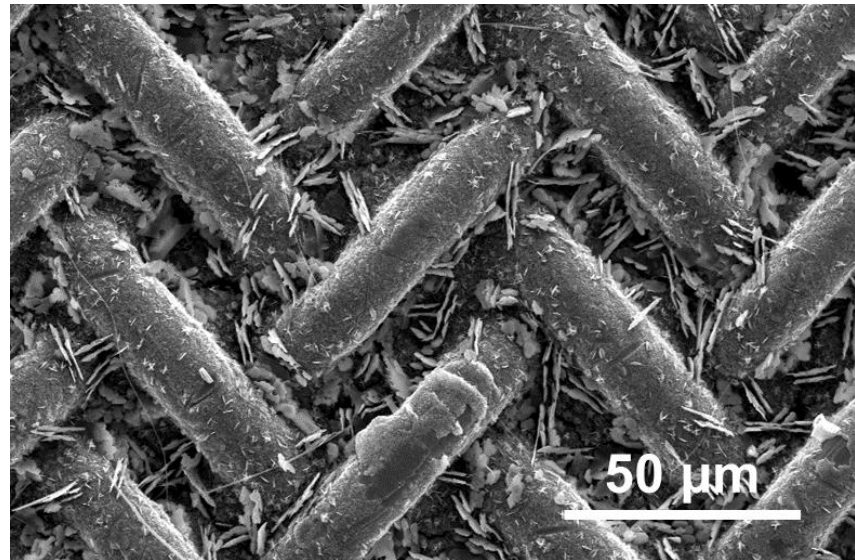


Fig. S18. SEM image of the AgVO cathode after discharging to 0.4 V in 3 M ZnSO_4 electrolyte in the first cycle.

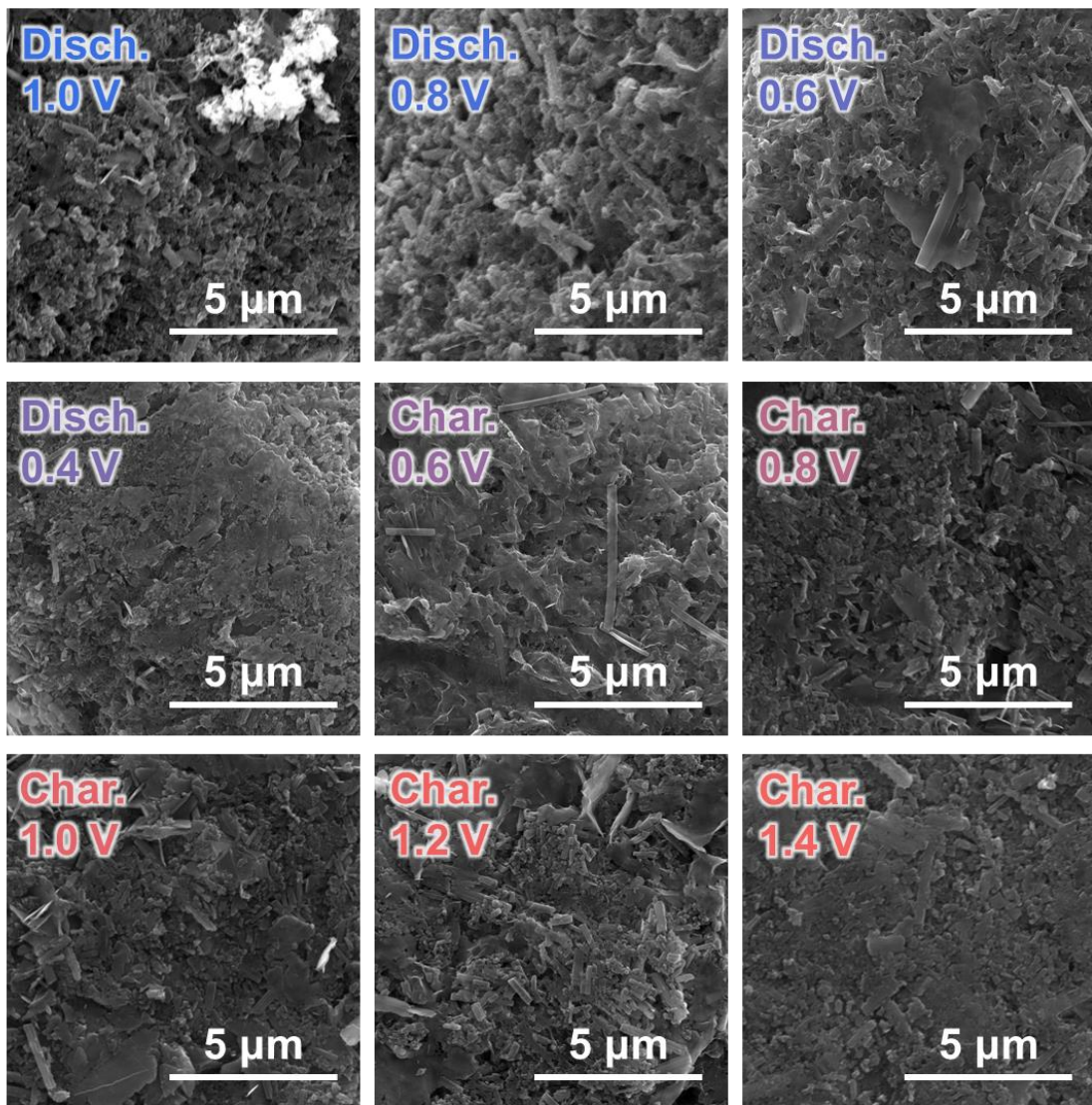


Fig. S19. *Ex situ* SEM images of AgVO cathodes in 3 M ZnSO₄ during the first cycle.

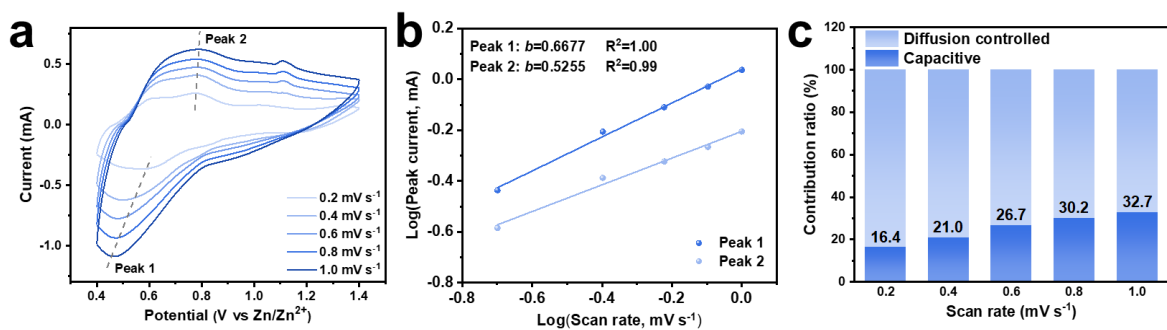


Fig. S20. (a) CV curves AgVO/Zn batteries at different scan rates ($0.2\text{--}1.0\text{ mV s}^{-1}$), (b) the calculated b-value of two redox peaks, and (c) corresponding capacitive contribution at different scan rates.

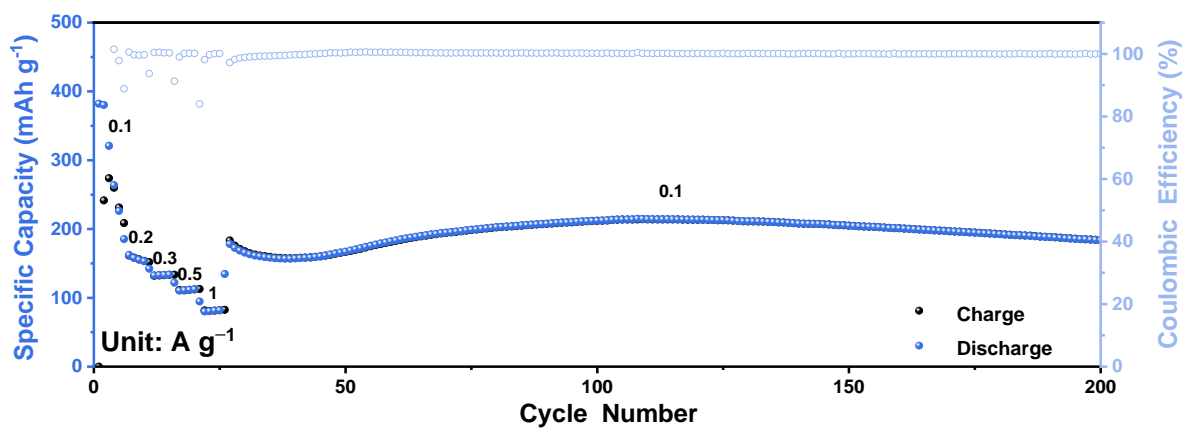


Fig. S21. Rate performance of AgVO/Zn batteries at different current densities.

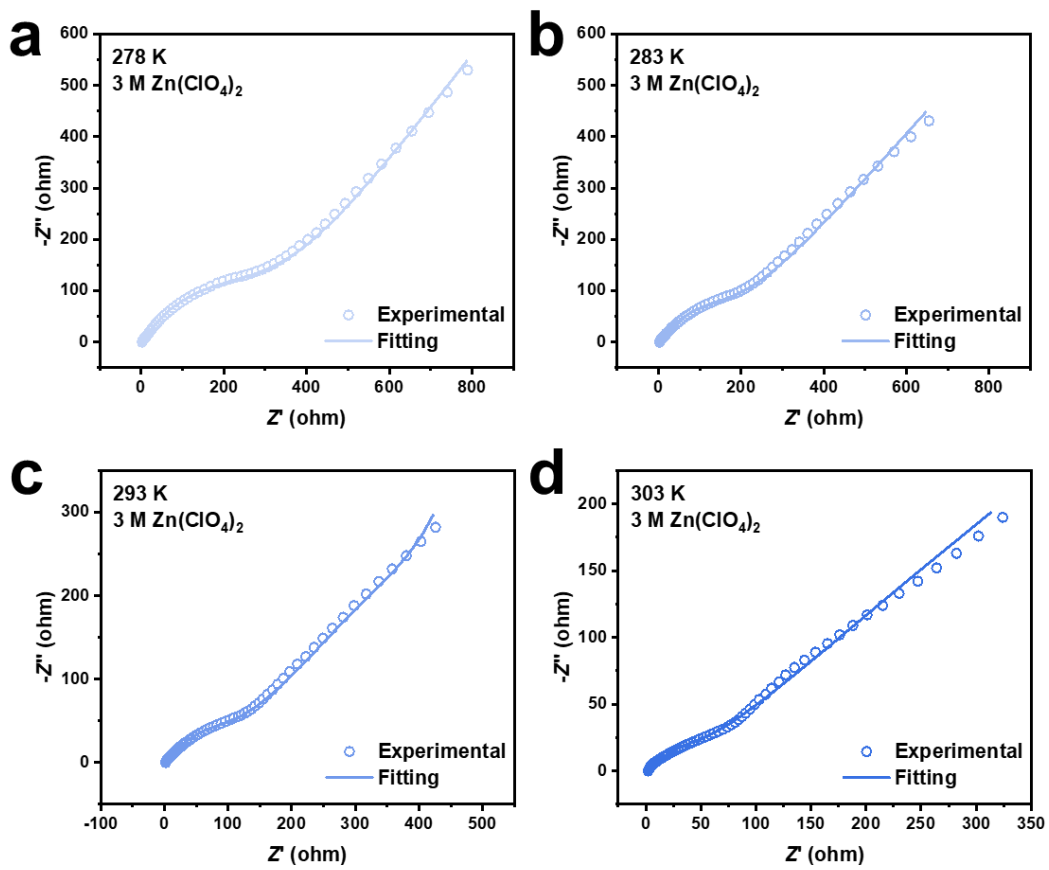


Fig. S22. Nyquist plots and fitting curves of the batteries in 3 M $\text{Zn}(\text{ClO}_4)_2$ at different temperatures at a fully charged state after 10 cycles at 0.1 A g^{-1} .

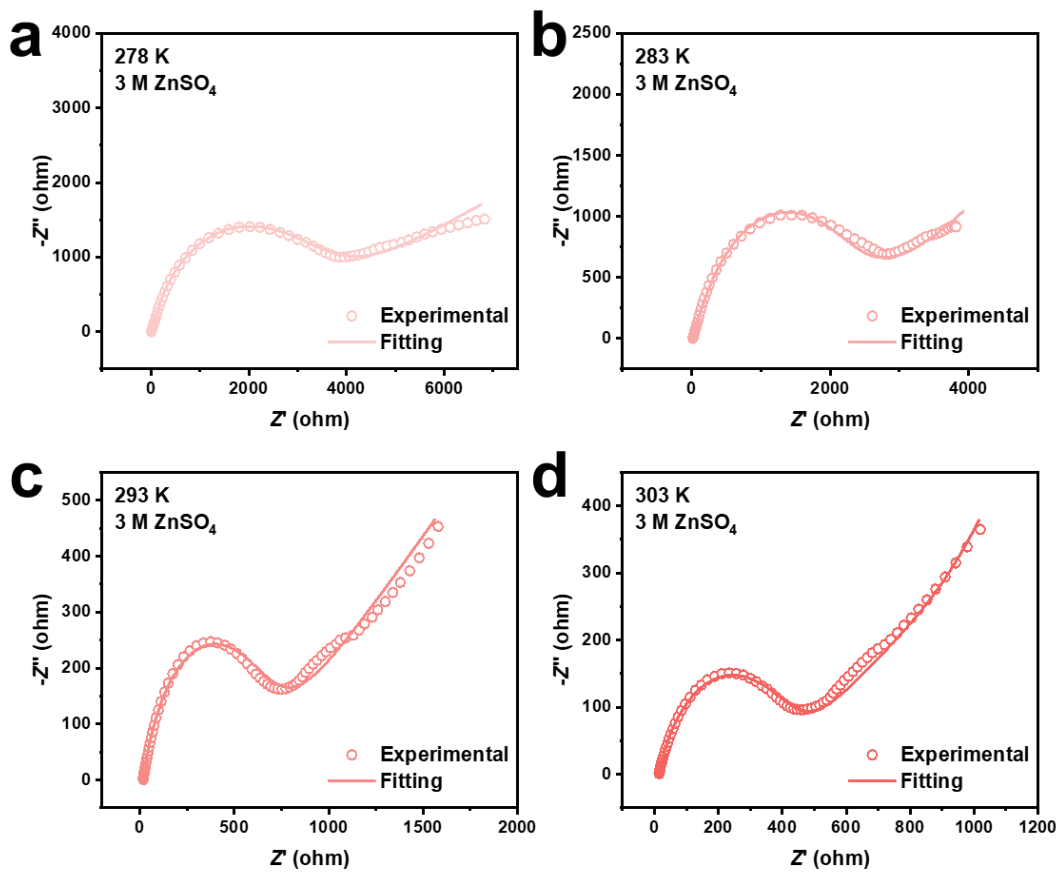


Fig. S23. Nyquist plots and fitting curves of the batteries in 3 M ZnSO_4 at different temperatures at a fully charged state after 10 cycles at 0.1 A g^{-1} .

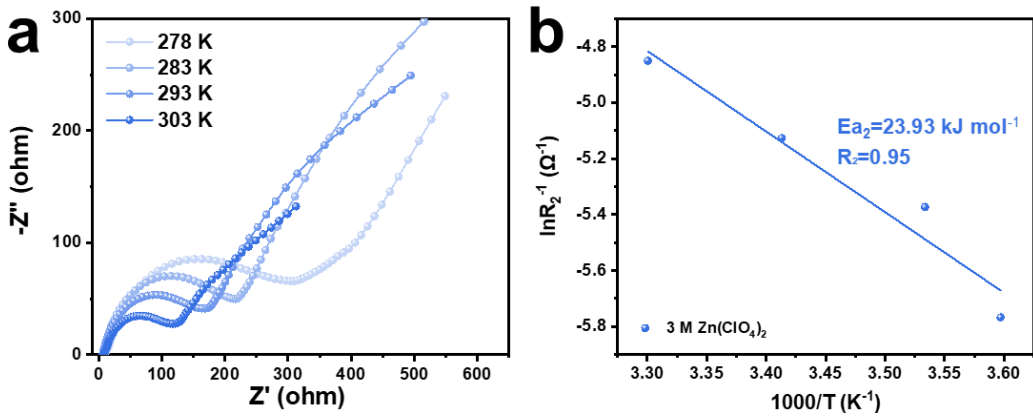


Fig. S24. (a) Nyquist plots of AgVO/Zn batteries in 3 M $Zn(ClO_4)_2$ without cycling at different temperatures. (b) The activation energy Ea_2 determined by the Arrhenius equation.

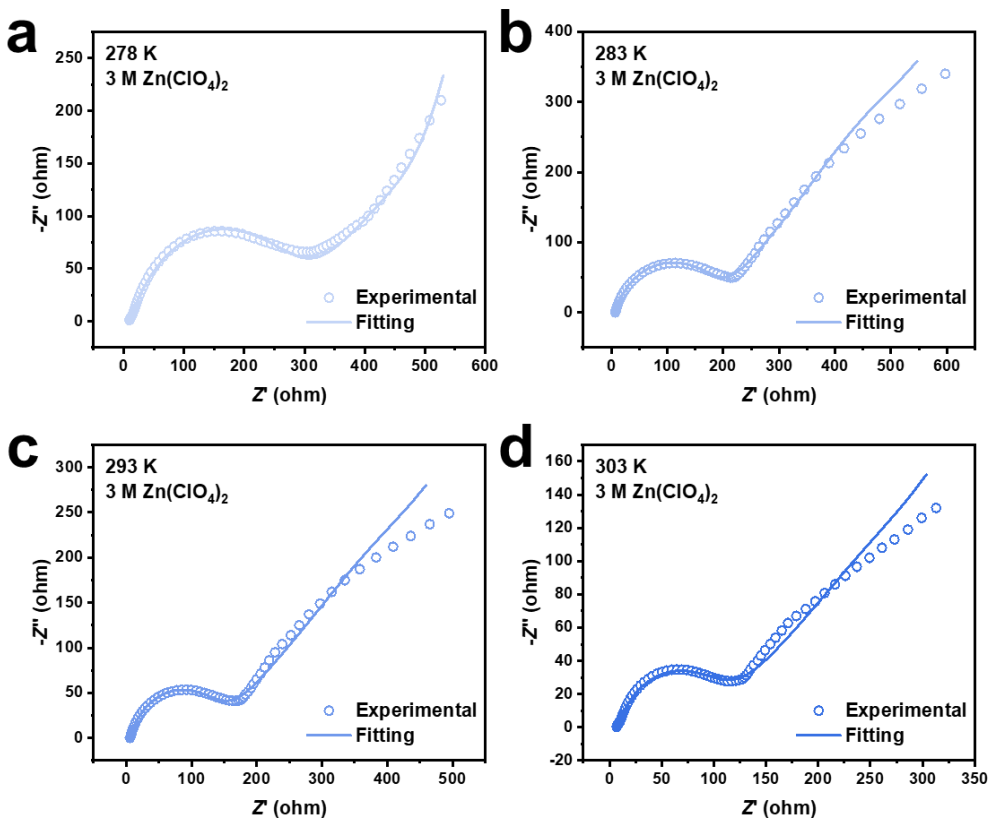


Fig. S25. Nyquist plots of the batteries without cycling in 3 M $\text{Zn}(\text{ClO}_4)_2$ at different temperatures.

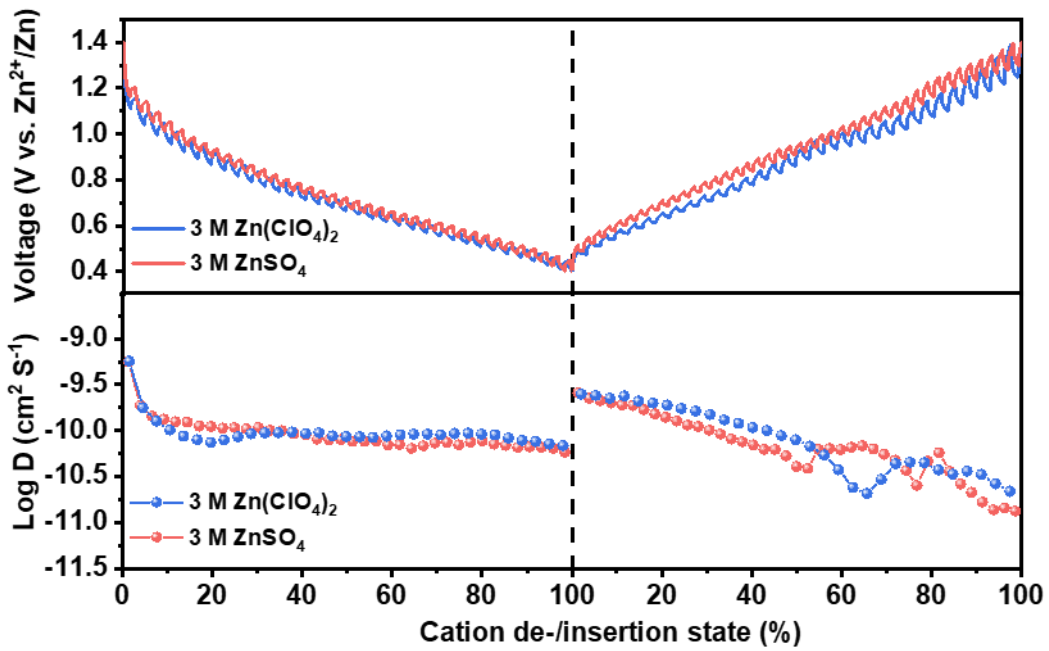


Fig. S26. Discharge/charge curves of GITT measurement and corresponding diffusion coefficients (D) of Zn^{2+} of AgVO cathode cycled in 3 M $\text{Zn}(\text{ClO}_4)_2$ and 3 M ZnSO_4 at the 5th cycle.

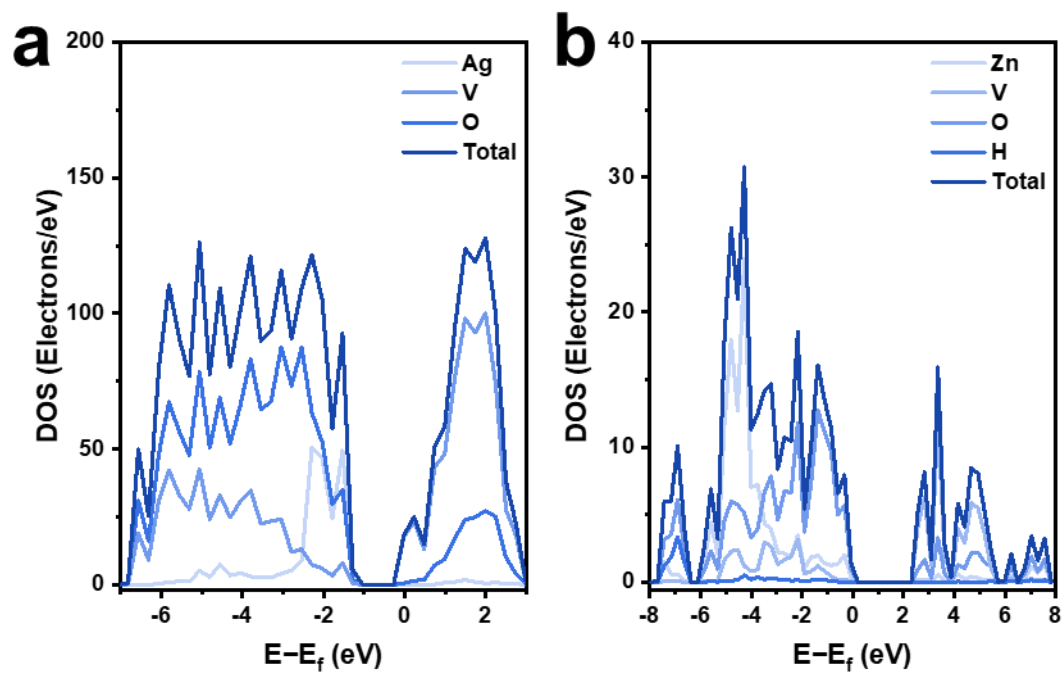


Fig. S27. DOS images of (a) AgVO and (b) ZnVO.

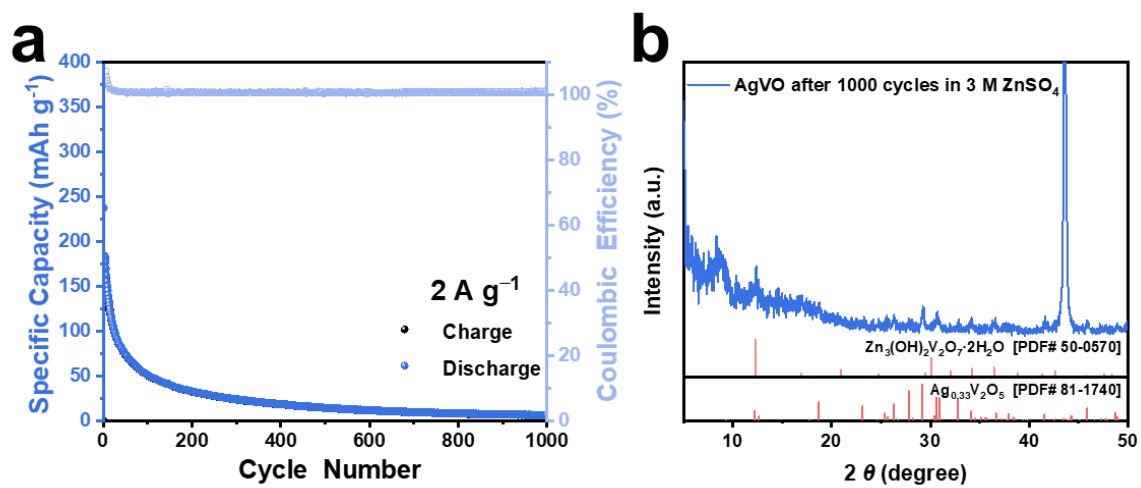


Fig. S28. (a) Cycling performance of AgVO/Zn battery in 3 M ZnSO_4 at 2 A g^{-1} for 1000 cycles.
(b) Corresponding XRD pattern of AgVO cathode after 1000 cycles.

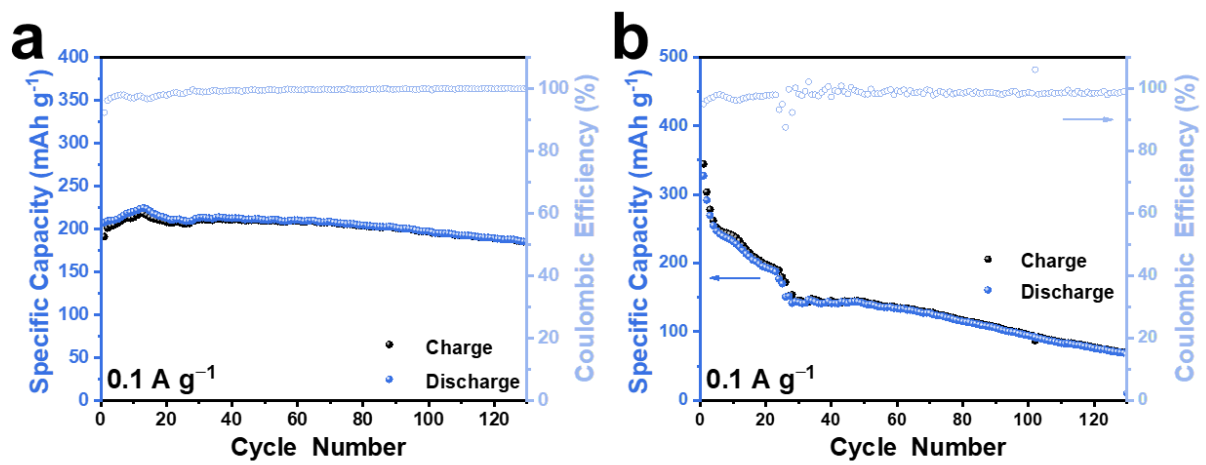


Fig. S29. Cycling performances of AgVO/Zn batteries at 0.1 A g^{-1} using (a) 1 M $\text{Zn}(\text{ClO}_4)_2/\text{PC}$ and (b) 3 M ZnSO_4 electrolytes.

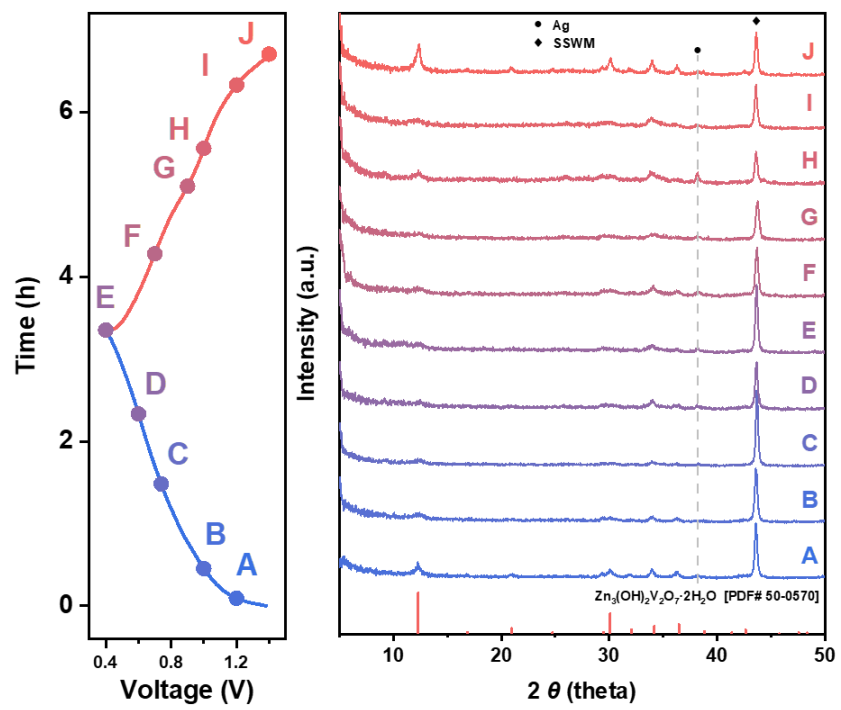


Fig. S30. *Ex situ* XRD patterns of the AgVO cathodes cycled in 3 M $Zn(ClO_4)_2$ electrolyte at the state D.

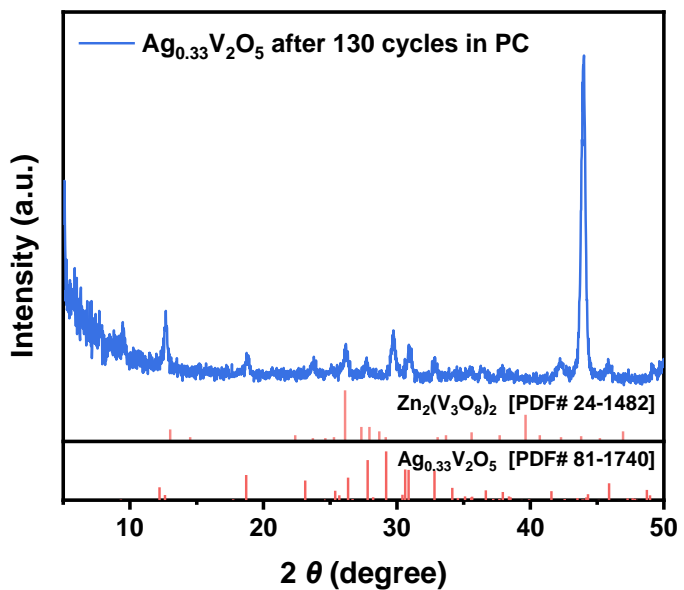


Fig. S31. XRD pattern of the AgVO cathode after cycling 130 cycles in 1 M $\text{Zn}(\text{ClO}_4)_2/\text{PC}$ electrolyte.

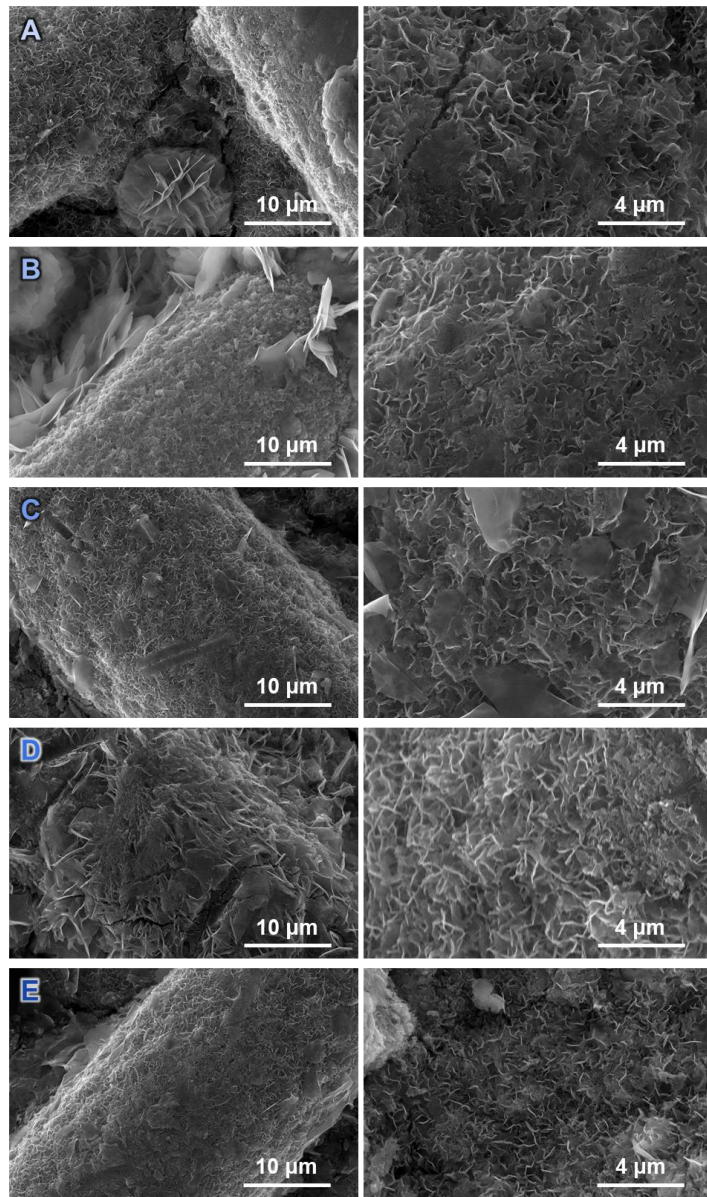


Fig. S32. SEM images of AgVO cathodes at different cycles.

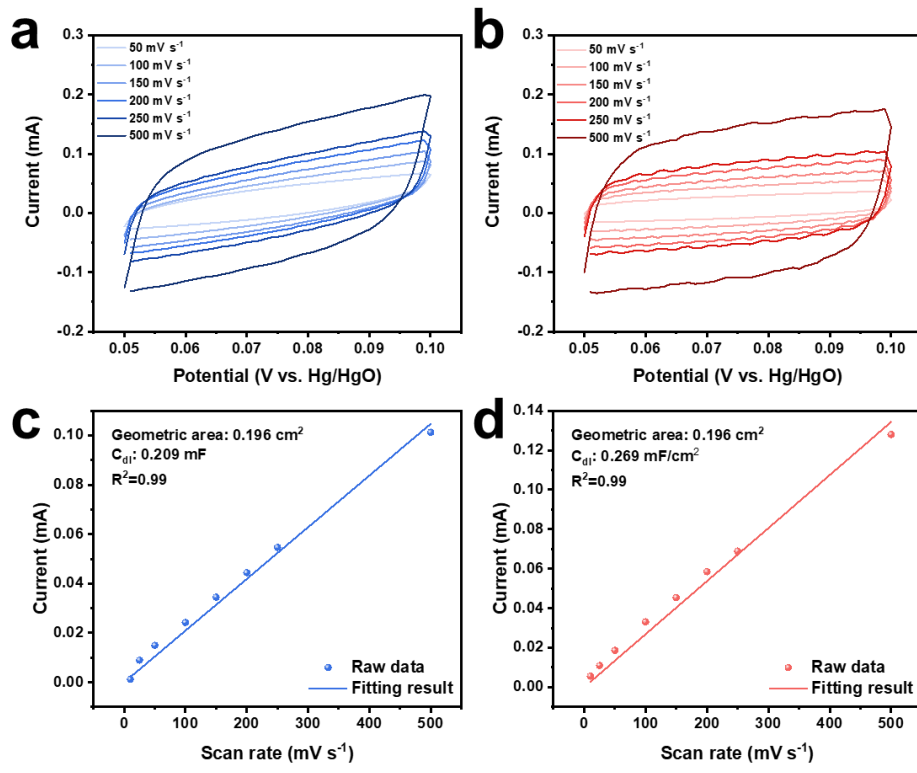


Fig. S33. CV curves in the non-faradaic region at various scan rates (10 to 500 mV/s) of the cathodes (a) before and (b) after state E. The corresponding plot of the current versus scan rate with the C_{dl} values from the linear fitting of the cathodes (c) before and (d) after state E.

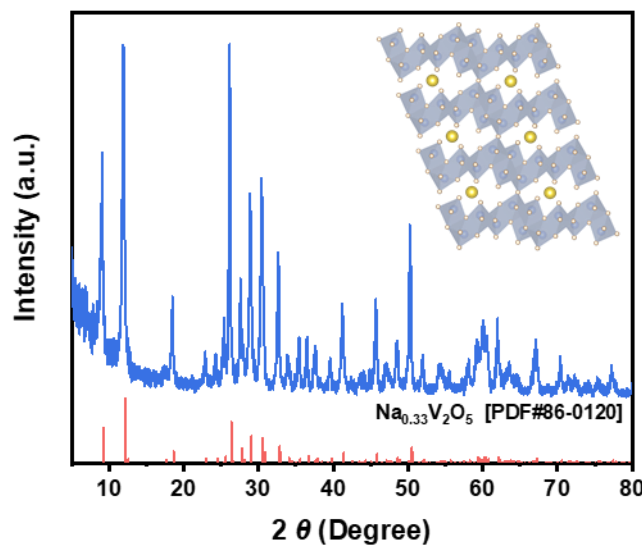


Fig. S34. XRD pattern and crystalline structure of as-synthesized NaVO.

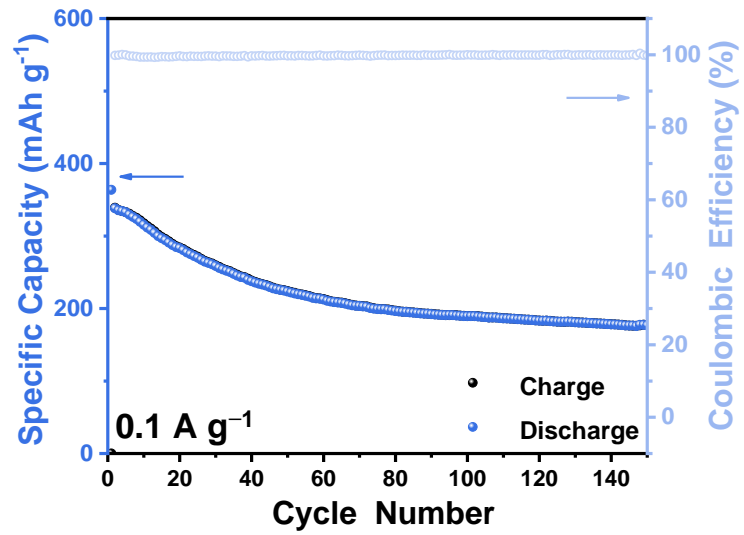


Fig. S35. Cycling performance of NaVO/Zn battery at 0.1 A g^{-1} .

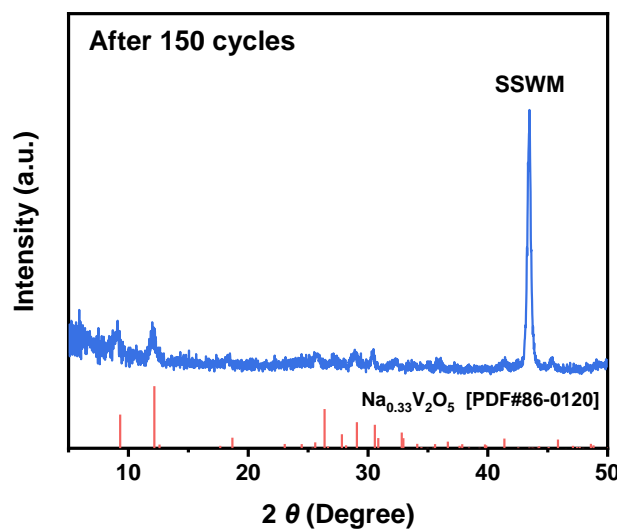


Fig. S36. XRD pattern of the NaVO cathode after cycling for 150 cycles at 0.1 A g^{-1} .

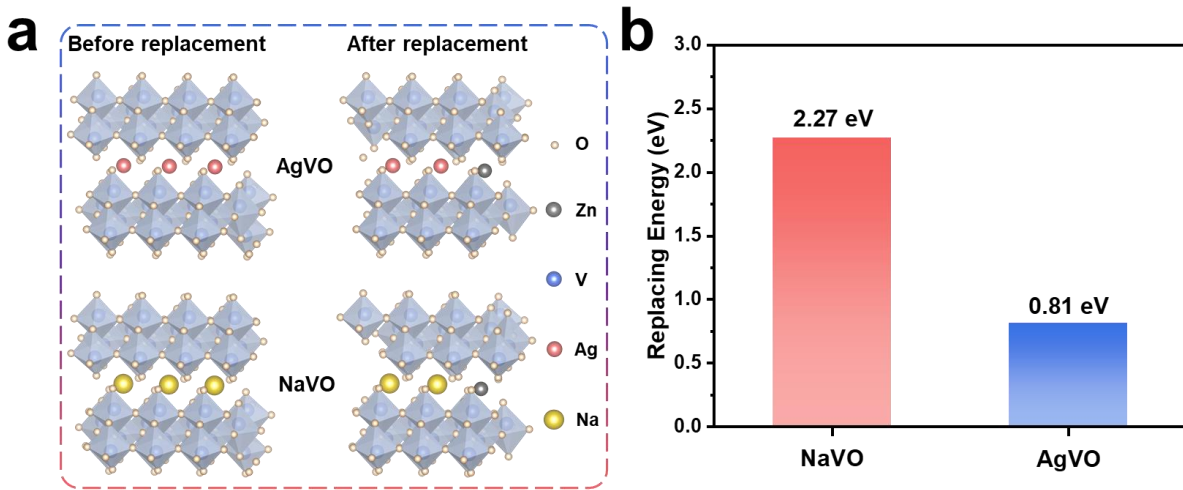
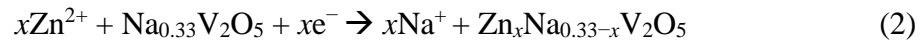
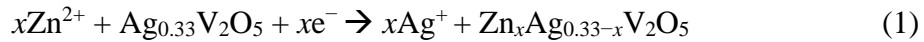


Fig. S37. (a) Processes of Zn^{2+} replacing Ag^{+} and Na^{+} in $AgVO$ and $NaVO$, respectively. (b) Corresponding replacing energies in both structures.

The replacing energies were calculated based on the following replacement reactions:



where x is the number of Zn^{2+} intercalated in both structures. In this process, the intercalation of Zn^{2+} induced the valence change in vanadium from +5 to +4, and the external circuit provides the same number of electrons as the intercalated Zn^{2+} to balance the charge in the crystalline system, corresponding to the XPS results in Fig. 1g.

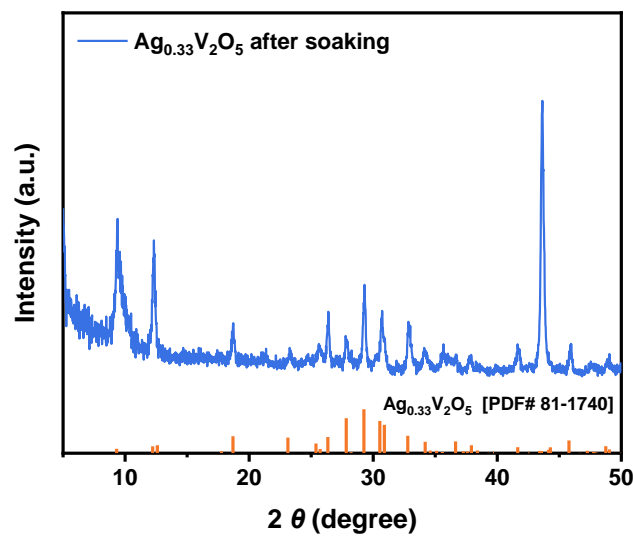


Fig. S38. XRD pattern of the AgVO cathode after soaking in 3 M $\text{Zn}(\text{ClO}_4)_2$ for ten days.

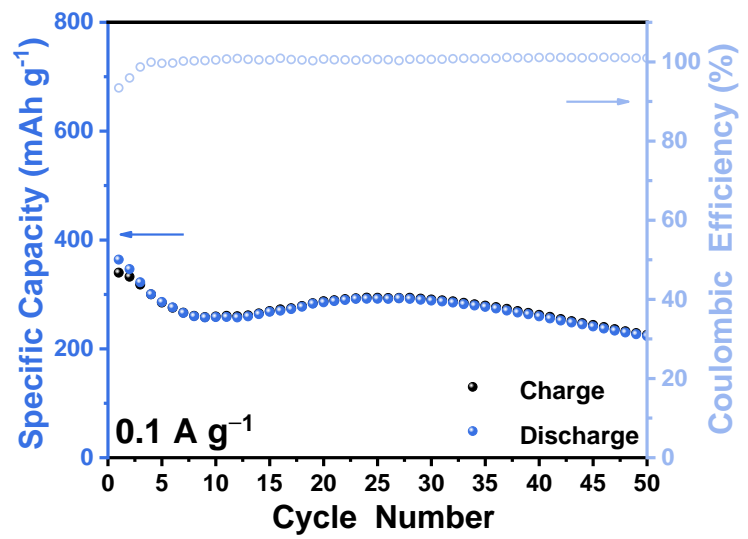


Fig. S39. Cycling performance of the soaked AgVO cathode at 0.1 A g^{-1} .

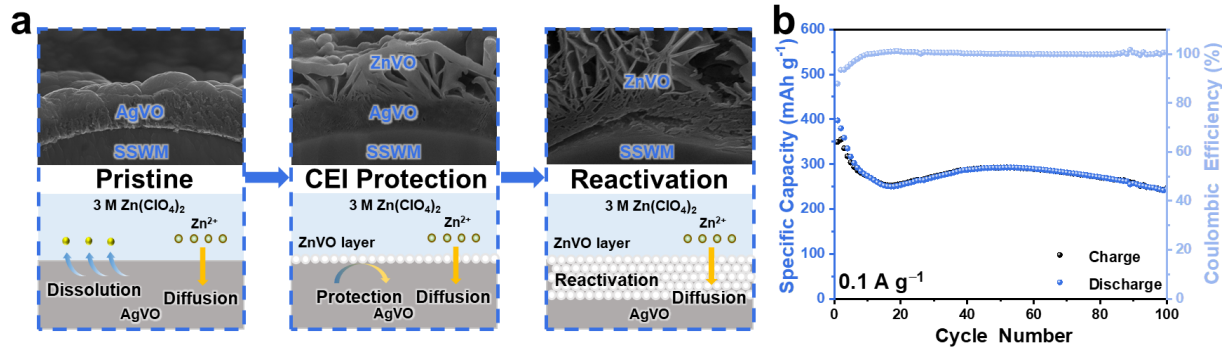


Fig. S40. (a) Schematic illustration of the mechanism of capacity reactivation of ZnVO. (b) Cycling performance of the AgVO/Zn pouch cell at 0.1 A g⁻¹.

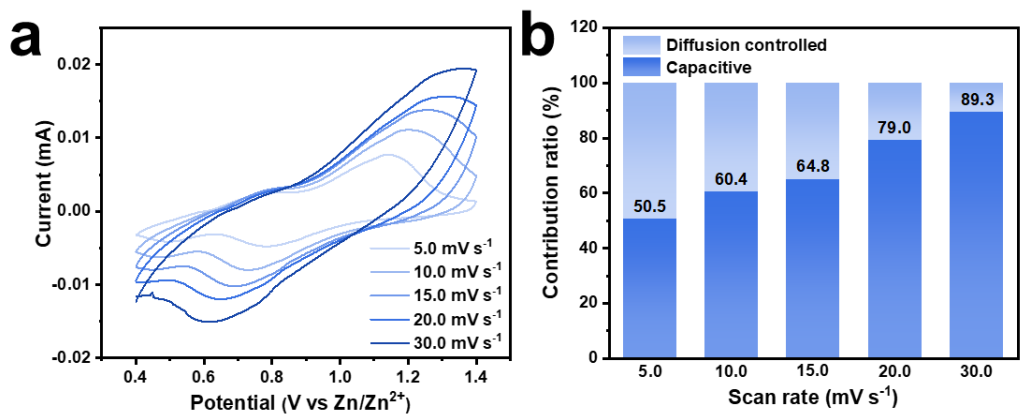


Fig. S41. (a) CV curves AgVO/Zn batteries after reactivation at different scan rates (5.0-30.0 mV s⁻¹) and (b) corresponding capacitive contribution at different scan rates.

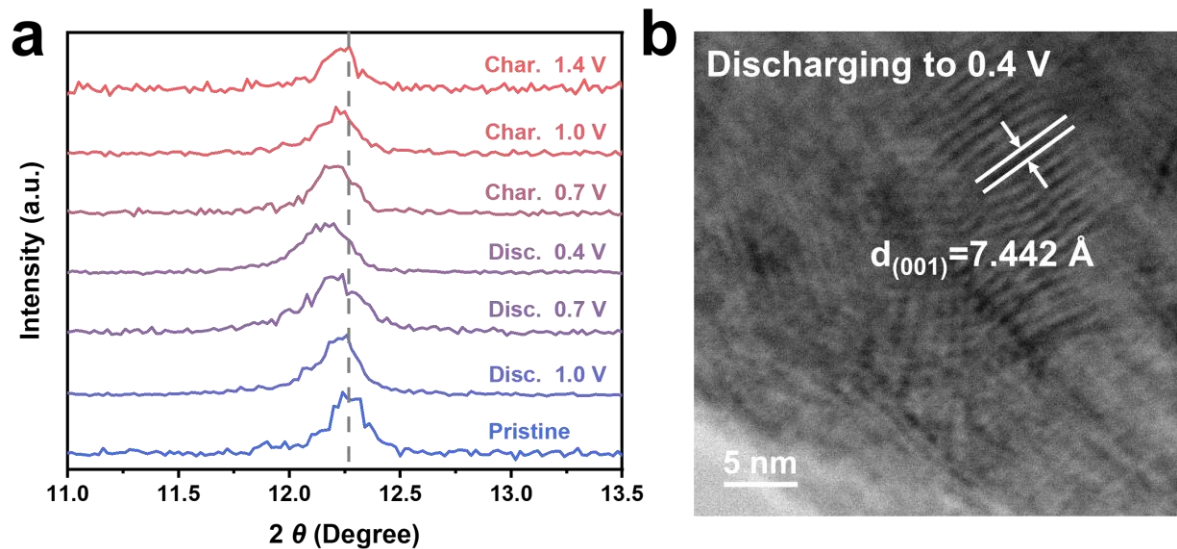


Fig. S42. (a) *Ex situ* XRD patterns of ZnVO cathodes at different states in the first cycle. (b) TEM image of ZnVO cathode after fully discharging to 0.4 V.

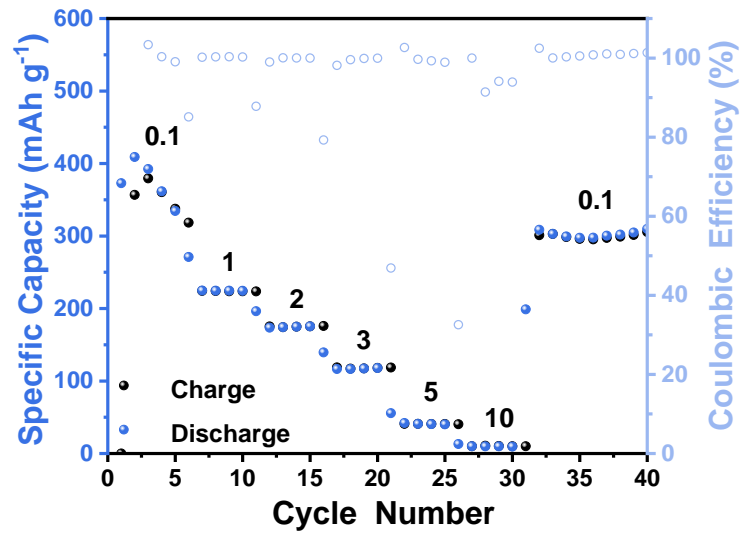


Fig. S43. Rate performance of AgVO/Zn battery in 3 M Zn(ClO₄)₂ electrolyte at different current densities without pre-activation.

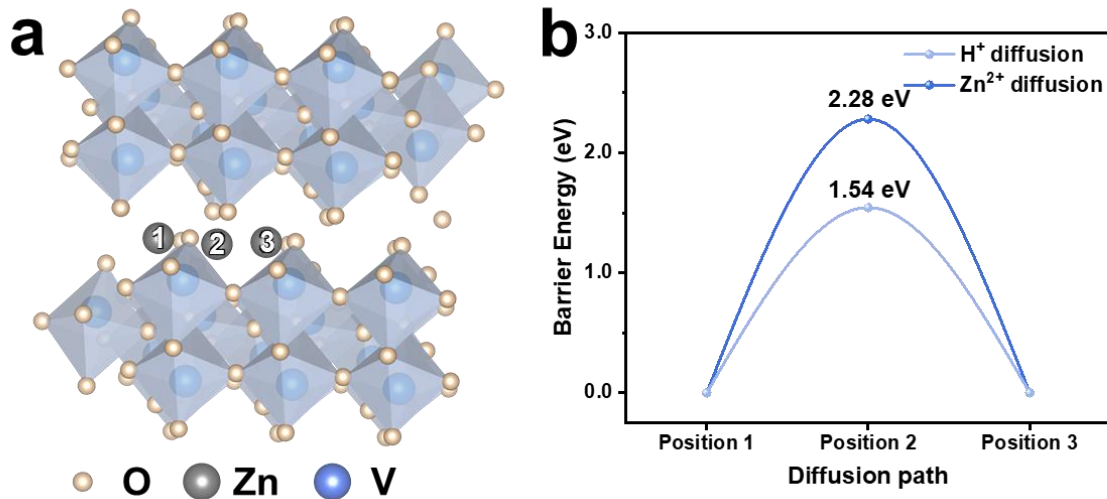


Fig. S44. (a) Possible diffusion pathways of Zn^{2+} in AgVO, and (b) corresponding diffusion energy barriers of Zn^{2+} and H^+ .

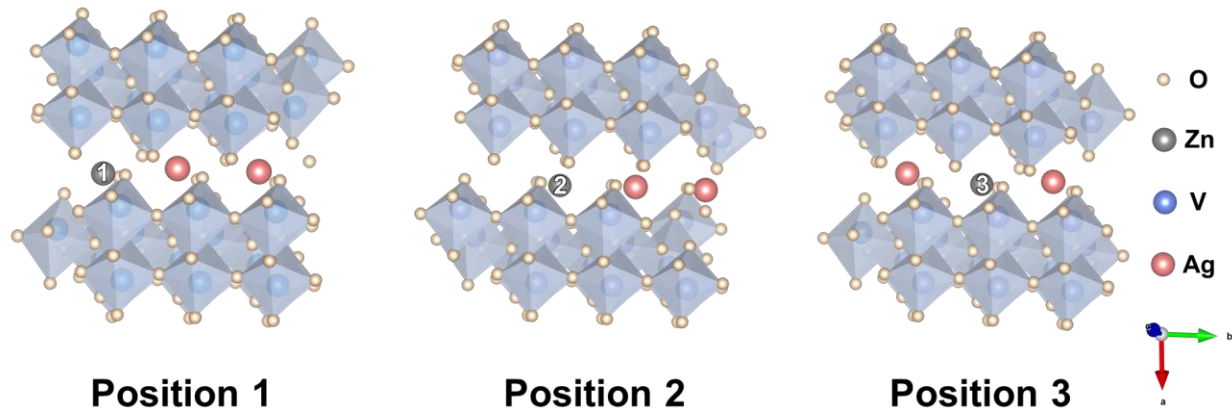


Fig. S45. Migration pathway of Zn^{2+} in AgVO .

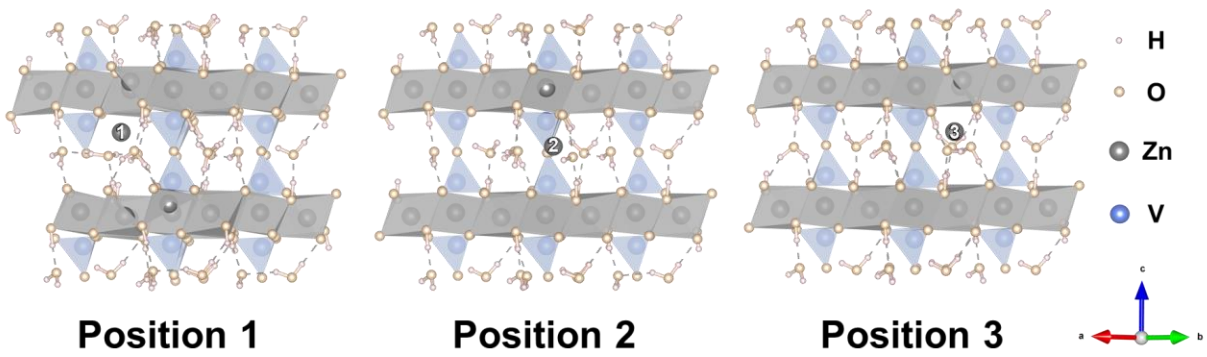


Fig. S46. Migration pathway of Zn^{2+} in ZnVO .

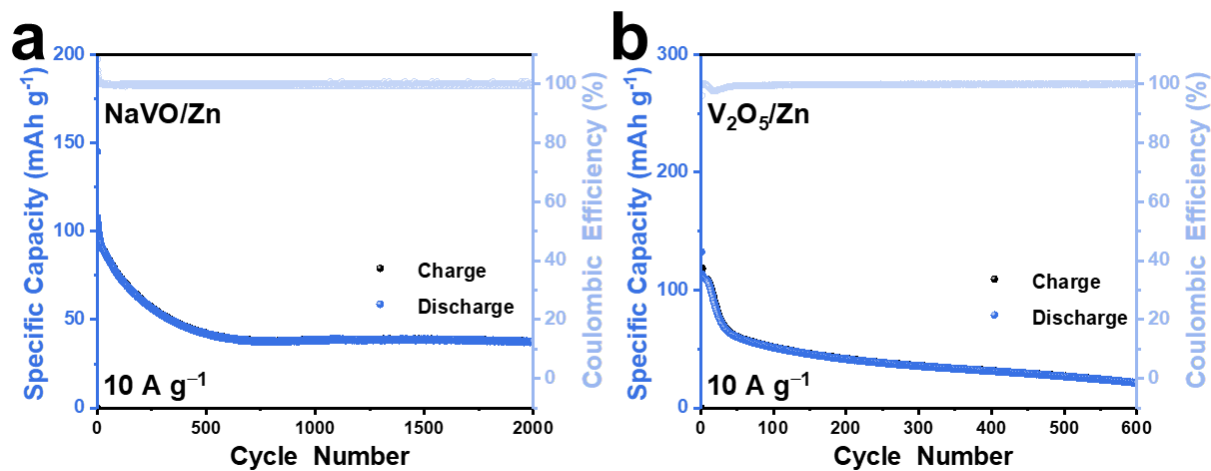


Fig. S47. Cycling performance of (a) NaVO/Zn and (b) $\text{V}_2\text{O}_5/\text{Zn}$ batteries in 3 M $\text{Zn}(\text{ClO}_4)_2$ electrolyte at 10 A g^{-1} .

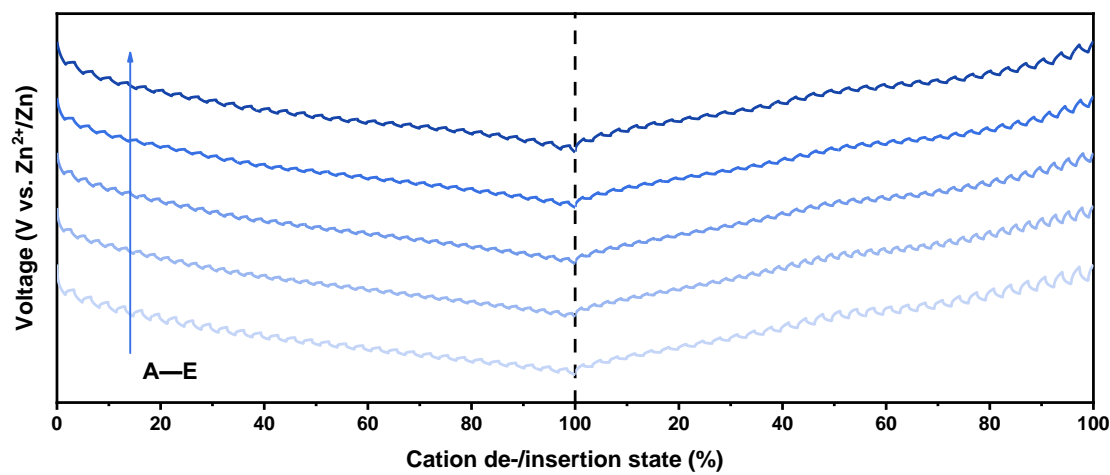


Fig. S48. (f) Discharge/charge curves of GITT measurement and (g) corresponding diffusion coefficients of Zn^{2+} after different cycles.

Supplementary tables:

Table S1. Concentrations (in ppm) of V analytes in 3 M ZnSO₄ electrolytes with different cathodes through solution mode ICP-MS

Samples in 3 M ZnSO ₄	Concentration of V (ppm)
Blank	0.00
5 cycles	130.19
10 cycles	93.41
20 cycles	121.91
30 cycles	132.55

Table S2. Concentrations (in ppm) of V analytes in 3 M Zn(ClO₄)₂ electrolytes with different cathodes through solution mode ICP-MS

Samples in 3 M Zn(ClO ₄) ₂	Concentration of V (ppm)
Blank	0.00
5 cycles	0.64
10 cycles	0.29
20 cycles	0.49
30 cycles	0.33

Reference:

- 1 P. He, G. Zhang, X. Liao, M. Yan, X. Xu, Q. An, J. Liu and L. Mai, *Advanced Energy Materials*, 2018, **8**, 1702463.
- 2 Z. Pan, J. Yang, J. Yang, Q. Zhang, H. Zhang, X. Li, Z. Kou, Y. Zhang, H. Chen, C. Yan and J. Wang, *ACS Nano*, 2020, **14**, 842–853.
- 3 Z. Wang, M. Zhou, L. Qin, M. Chen, Z. Chen, S. Guo, L. Wang, G. Fang and S. Liang, *eScience*, 2022, **2**, 209–218.
- 4 Y. J. Son, K. Kawashima, B. R. Wygant, C. H. Lam, J. N. Burrow, H. Celio, A. Dolocan, J. G. Ekerdt and C. B. Mullins, *ACS Nano*, 2021, **15**, 3468–3480.
- 5 C. C. L. McCrory, S. Jung, J. C. Peters and T. F. Jaramillo, *J. Am. Chem. Soc.*, 2013, **135**, 16977–16987.
- 6 G. Fang, C. Zhu, M. Chen, J. Zhou, B. Tang, X. Cao, X. Zheng, A. Pan and S. Liang, *Advanced Functional Materials*, 2019, **29**, 1808375.
- 7 D. T. Ngo, H. T. T. Le, C. Kim, J.-Y. Lee, J. G. Fisher, I.-D. Kim and C.-J. Park, *Energy Environ. Sci.*, 2015, **8**, 3577–3588.
- 8 S. Guo, S. Liang, B. Zhang, G. Fang, D. Ma and J. Zhou, *ACS Nano*, 2019, **13**, 13456–13464.
- 9 D. Fang, F. He, J. Xie and L. Xue, *Journal of Wuhan University of Technology-Mater. Sci. Ed.*, 2020, **35**, 711–718.
- 10 Z. Wang, M. Zhou, L. Qin, M. Chen, Z. Chen, S. Guo, L. Wang, G. Fang and S. Liang, *eScience*, 2022, **2**, 209–218.
- 11 W. Wang, V. S. Kale, Z. Cao, Y. Lei, S. Kandambeth, G. Zou, Y. Zhu, E. Abouhamad, O. Shekhah, L. Cavallo, M. Eddaoudi and H. N. Alshareef, *Advanced Materials*, 2021, **33**, 2103617.